OCEAN-ACOUSTIC SOLITARY WAVE STUDIES AND PREDICTIONS

A. C. WARN-VARNAS, S. A. CHIN-BING, D. B. KING and Z. HALLOCK
Naval Research Laboratory, Stennis Space Center, MS 39529, U.S.A.

J. A. HAWKINS
Planning Systems Inc., Slidell, LA 70458, U.S.A.

(Received 4 October 2000; Accepted 26 March 2002)

Abstract. Shallow water internal solitary waves have become a major topic of interest to oceanographers and acousticians. In this paper we review the cross-disciplinary status of joint ocean-acoustic solitary wave studies and predictions. We consider the process of acoustical mode coupling in the presence of solitary waves and the corresponding acoustical intensity loss due to increased coupling with the bottom. A study of the interaction of an acoustical field with a train of solitary waves is undertaken at a range of frequencies. At a resonant frequency the acoustic field can interact with the solitary wave packet which results in mode conversions (acoustic energy is redistributed among the modes, often from lower-order to higher-order modes). Higher signal losses can occur in the higher order modes through increased bottom attenuation and result in an anomalous acoustical intensity loss at the resonant frequency.

We present some new results of joint ocean-acoustic research, from a dedicated study in the Strait of Messina, where solitary waves are generated by semidiurnal tidal flow over topographic variations. The University of Hamburg weakly nonhydrostatic two layer model is used for simulating the generation and propagation of solitary waves. In particular, the physical states encountered during an October 1995 cruise in the Strait of Messina (between Italy and Sicily) are simulated. Various parameter space sensitivity studies, about the existing cruise conditions, are performed. The modelled solitary wave trains are compared against conductivity-temperature-depth (CTD) chain measurements in terms of amplitudes, wavelengths, phase speeds and correlations with data. Predicted and observed sound speeds are used in acoustical intensity calculations that are conducted with a parabolic equation (PE) model. The differences in the resultant acoustical intensity fields provide a guide for the tuning of the oceanographic model parameters. The tuned oceanographic model shows agreement with data for the first and second solitary waves in terms of amplitude, wavelength and phase speed. The calculated available potential energy from the simulation results is in the range of the data analogue.

Keywords: acoustical intensity, acoustical modes, dispersion, internal solitary waves, ocean-acoustic, resonance.

1. Introduction

The motivation for joint ocean-acoustic studies of internal solitary waves was provided by the observation of an anomalous frequency response in shallow-water sound propagation measurements. In particular, acoustical measurements in the Yellow Sea conducted by Zhou et al. (1991) showed an anomalous drop in acoustical intensity, of about 20 dB, at a range of 28 km for acoustic frequencies around

Surveys in Geophysics **24:** 39–79, 2003.

630 Hz. The measured transmission loss was found to be time and direction dependent. The authors performed transmission loss calculations using an acoustic parabolic equation (PE) model and used a gated sine function to represent solitary waves in the thermocline. The simulation results from this hypothetical case showed that an anomalous transmission loss could occur at a frequency of around 630 Hz when acoustical waves and solitary waves interact. Computer simulations subsequently confirmed (Chin-Bing et al., 1993; King et al., 1994) that the resonant like transmission loss is caused by an acoustical mode coupling due to the presence of solitary waves, together with a corresponding larger bottom attenuation for the coupled acoustic modes. At the resonant frequency (630 Hz) acoustic modes are coupled and energy is passed from one mode to another. When the acoustic mode receiving the energy has a higher bottom attenuation than the other acoustic mode, a net loss in transmitted energy occurs. Over a long distance these losses become additive and result in a large transmission loss. The entire process resembles a resonance phenomenon (Chin-Bing et al., 1993; King et al., 1994).

The temporal and spatial scales of tidally induced internal bores and solitary waves are such that they can have a significant effect on the acoustic field through the sound speed structure. At certain frequencies the interaction of the acoustical field with the solitary wave train can be quite significant. Many interactions of the acoustical field with the solitary wave train can occur between the source and receiver.

Duda and Preisig (1999) investigated theoretically the coupling of acoustical normal modes in the presence of solitary wave type disturbances. They found that the transfer of energy between acoustical modes is caused by strong lateral gradients of sound speed in the waves. The mode phasing within the solitary wave packet varies with time scales of minutes, causing coupling and signal fluctuations at comparable time scales.

Since the Zhou et al. (1991) studies, littoral acoustical and oceanographic experiments have been conducted on the synoptic and local scales. In these experiments fronts, eddies, mesoscale variability, tidal effects, internal waves, and solitary waves were present. Surveys have been performed on the New Jersey and New England continental shelves. During the summer of 1995 the SWARM (shallow water acoustics in a random medium) survey (The SWARM Group, 1997) was conducted on the continental shelves region of the New Jersey coast (Apel et al., 1998). The 1996 and 1997 Shelfbreak PRIMER experiments (The Shelfbreak PRIMER Group, 1997) addressed an integrated acoustic and oceanographic field study in the middle Atlantic bight region.

On the Malin shelf-edge, on the North-West UK shelf margin, the Shelf Edge Study Acoustic Measurement Experiment (SESAME) took place in August-September 1995 and 1996 (Small et al., 1999; Hallock, 2000). In the Strait of Gibraltar, Tieman et al. (1999) conducted an acoustic monitoring experiment, in April of 1996, to measure the effects of passing internal bores. They used acoustic propagation models to interpret and understand the observations.

Analysis of the SWARM data has shown acoustic field fluctuations in the thermocline region caused by solitary wave packets (Finette et al., 1999). The time variations in intensity and phase are attributed to acoustic mode coupling. An analysis of mode coupling due to solitary waves and their effects on modal intensity statistics has been performed by Tielburger et al. (1997).

Analysis of the SESAME data, also, shows a decrease in acoustical intensity caused by a solitary wave packet (Field, 2000, unpublished). The preliminary results indicate an intensity decrease of around 5 to 6 dB at 800 Hz.

Internal tides are generated by the interaction of the barotropic tide with stratification in the presence of rapidly changing topography. Baines (1973, 1982) has demonstrated the generation process analytically. New (1988) has modelled the generation process in the presence of steep linear slopes. Sherwin (1991) has investigated numerically the effects of semi-diurnal tidal fluctuations on acoustic intensity at a steep shelf edge. The tidally induced uplifting and down lifting of the isopycnals and sound speed caused acoustical energy losses in the range of 5 dB to 15 dB depending on bottom loss assumptions.

The generation and propagation of solitary waves have been modelled with nonhydrostatic hydrodynamic models. Hydrodynamic modeling of tidal flow over steep topography shows that the tidal flow depresses the thermocline and generates an internal bore (Lamb, 1994; Brand et al., 1997). The internal bore propagates and its leading edge steepens through nonlinear effects. The region where the leading edge steepens over topographic variations corresponds to a location where the flow becomes supercritical because it gets trapped there (as it can no longer propagate against the current) during the semidiurnal tidal flow reversal. Then frequency and amplitude dispersion sets in and the leading edge disintegrates into solitary waves that propagate (Lamb, 1994; Brand et al., 1997).

In the Strait of Messina numerical simulations have been performed with a two layer model by Brand et al. (1997) and Warn-Varnas et al. (1999). In the Georges Bank area, solitary waves were simulated at the shelf break with a terrain following sigma-coordinate model by Lamb (1994). Some preliminary solitary wave simulations have been conducted in the Yellow Sea for idealized topography by Warn-Varnas et al. (1999). In these models the barotropic semidiurnal tidal flow is prescribed at the boundaries. This in turn leads to the generation of internal tides by the interaction of the flow (induced by barotropic tides) with stratification in presence of strong topographic variations.

The hydrodynamic or Korteweg-de Vries (KdV) types of solitary wave models are coupled to acoustical models through the sound speed predictions. The sound speed is used in acoustical field calculations. Ocean dynamical variability such as internal bore or solitary wave propagation is reflected in sound speed variability. The acoustical field intensity is calculated with parabolic equation models (PE) for given configurations of source, receiver, frequency, and bottom loss. Finette et al. (1999) used a KdV type model to predict the sound speed for the 1994 SWARM experiment.

In the Strait of Messina, the authors of this paper have performed a joint ocean-acoustic study of solitary waves and their effects. There the various elements of joint ocean-acoustics modelling are present and can be pursued in an unhindered manner because of the certainty that the solitary wave trains are present during the semidiurnal tidal cycle. The solitary wave structure was predicted with the University of Hamburg weakly nonhydrostatic two-layer model (Warn-Varnas et al., 1999). The sound speed was derived from the hydrodynamic model predictions and coupled to an acoustical PE model. Chin-Bing et al. (1999) performed acoustical transmission loss calculations with a PE model using measured and predicted sound speed distributions containing solitary wave variability.

The hydrodynamic solitary wave predictions were compared and validated against measurements. The model parameters were tuned to obtain the best agreement between predicted and measured solitary wave structure. In the future we hope that joint ocean-acoustic measurements will be available to extend the joint ocean-acoustic predictions by validation against measurements and the inclusion of relevant ocean-acoustic phenomena. This paper is organized into sections on solitary wave train interaction with the acoustic field, ocean-acoustic modeling, Strait of Messina data and analysis, parameter space studies, comparison of simulated oceanographic fields with data, potential energy distributions, ocean-acoustic predictions and perspective, and a summary.

2. Solitary Wave Train Interaction with the Acoustic Field

2.1. Oceanographic and acoustic scales

A train of solitary waves can be characterized by wavelength scales of the order of 10^3 m. The phase speed can be around 1 m/s, amplitude 50 m, and frequency 10^{-3} Hz. The individual wavelengths, amplitudes, and phase speeds vary in a solitary wave train itself and in the different regions of the world oceans where solitary waves are found.

On the acoustical side we are dealing with frequencies of a few hundred to few thousand Hz. At a frequency of 1000 Hz the wavelength is 1.5 m for an ocean sound speed of 1500 m/s. The acoustical propagation speeds and frequencies are orders of magnitude higher than the corresponding oceanographic analogue.

The speed of sound in the ocean usually does not vary by more than 100 m/s from the nominal value of 1500 m/s. With regard to scales of magnitude, the sound speed in ocean water can be regarded as constant (1500 m/s), and, therefore, the acoustic wavelength is inversely proportional to the frequency of the acoustic wave. In the range of 100 Hz to 2 kHz, the acoustical wavelengths are orders of magnitude smaller than the oceanographic counterparts. The comparably shorter acoustical wavelengths in relation to the solitary wave wavelengths enable the acoustical field to interact with the solitary wave distribution located between source and receiver.

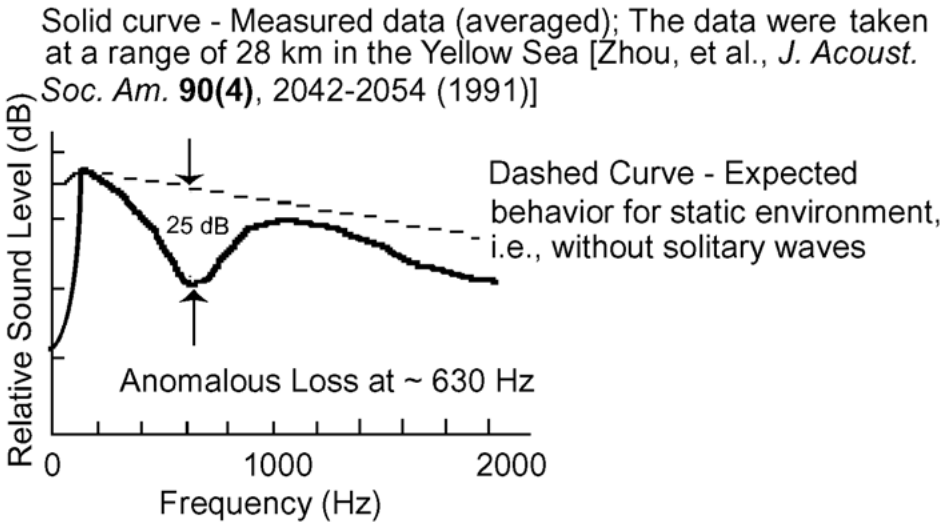

Figure 1. Sketch of the results published by Zhou et al. (1991).

As a result many interactions of the acoustical field and the solitary wave train can occur. The differences in scenarios with and without solitary wave disturbances in the acoustical path can be striking. The following sections discuss the consequences of the solitary wave train's interactions with the acoustical field.

2.2. ANOMALOUS LOSS OF ACOUSTICAL INTENSITY

Zhou et al. (1991) have measured the frequency response of sound propagation in an area of the Yellow Sea, which, from their description, we estimate is located south of the Shandong peninsula. The data were collected during various times of the year over a period of four years. The source and receiver were located below the strong summer thermocline. They published a plot of their measured power spectrum vs. frequency at a range of 28 km. We have sketched the essence of their results in our Figure 1. Their data show an anomalous drop in acoustical intensity at around 630 Hz; on the sound level axis, the tick marks are 20 dB apart.

Acoustic transmission loss calculations, with no representation of solitary waves, did not show an anomalous drop in acoustical intensity at 630 Hz. When, however, a hypothetical gated sine function representation of a solitary wave train was postulated in the thermocline, as shown in Figure 2, the acoustic model calculation showed a drop of acoustical intensity at around 630 Hz in agreement with the data. This very good agreement between data and acoustic model prediction was surprising and initiated a decade of ocean-acoustic investigations into the acoustic effects of shallow water solitary waves. The physical mechanism for the resonant loss of acoustical intensity at a particular frequency (frequency at which maximum attenuation occurs) can be understood in terms of mode coupling and

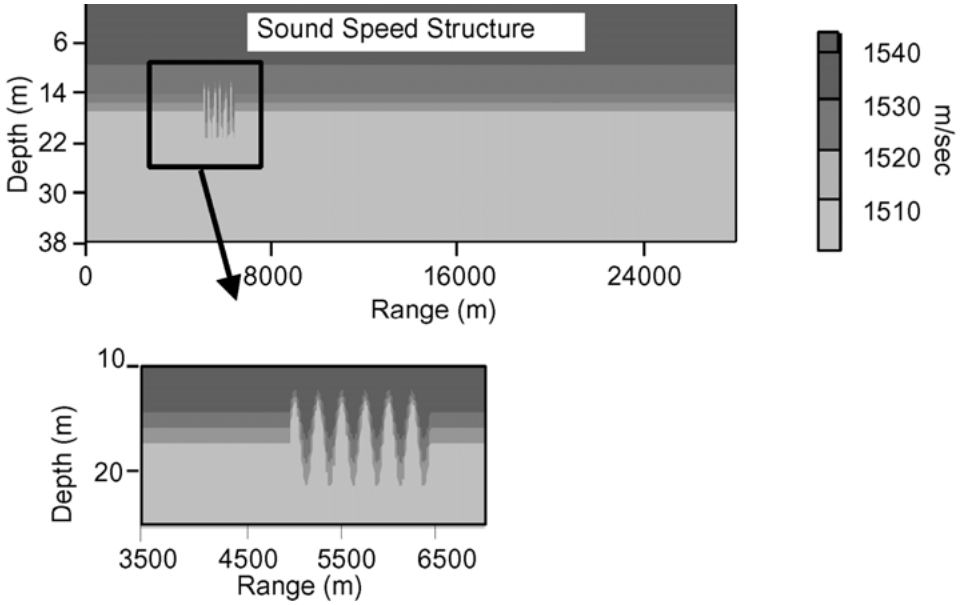

Figure 2. Representation of the solitary wave train used by Zhou et al. (1991).

energy redistribution among the normal (propagating) modes. A representation in terms of the normal modes can be calculated from the acoustic data generated by the PE model. This is done by decomposing the PE complex pressure field into wave number space by using a Fourier transform. The wave numbers are the modal eigenvalues. An illustration of this is shown in Figure 3. The top figure shows the decomposition of the field for an environment with a solitary wave (dotted line) and an environment without a solitary wave. The acoustic fields were created at a frequency (780 Hz) where resonance does not occur. Each peak represents a mode where its wavenumber is the modal eigenvalue and the amplitude is representative of the energy carried in each mode. Note that there is little difference in the amplitude of the mode either with or without the solitary wave. The dominate mode intensities are virtually unchanged when the solitary wave is placed between source and receiver (dashed curve). However, near and at the resonant frequency, the redistribution of energy among the modes is quite different when the solitary wave train is present between source and receiver (Figure 3, lower). The presence of the solitary wave train results in acoustic mode coupling, redistributing energy from the lowest-order mode (mode 1) into higher-order modes (modes 2, 3, 4, 5, 6, and 7). The simulation modeling results shown in Figure 3 are our duplication of the acoustic modeling analysis done by Zhou et al. (1991).

The Finite Element Parabolic Equation (FEPE) model (Collins, 1988a,b,c; 1989a,b,c; 1990a,b) was used to produce the simulations shown in Figure 3. The FEPE model uses improved energy conservation techniques (Collins, 1991; Collins and Westwood, 1991) and other techniques to produce a very accurate result. For a

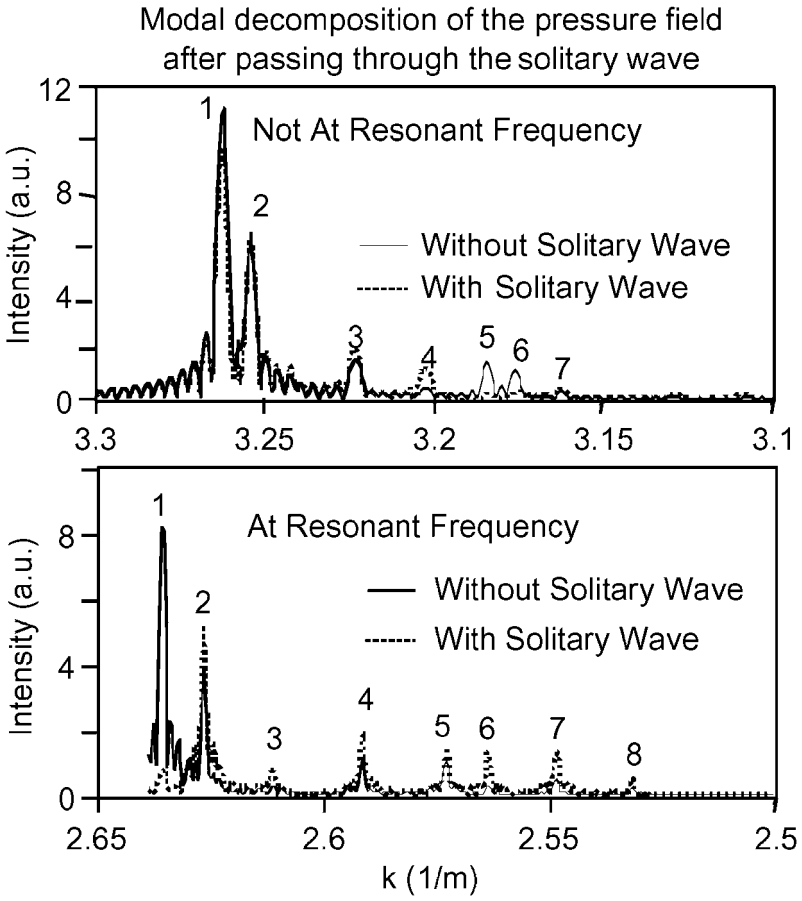

Figure 3. These figures are the result of Fourier transforming the acoustic model spatial results to wave number space. The peaks represent the acoustic modes (the wavenumber k is the modal eigenvalue) and the amplitude represent the amount of energy in each mode. The top result was done at a non resonance frequency of 780 Hz and the bottom panel was done at a frequency of 630 Hz.

more detailed look at the PE model physics the reader is directed to Appendix B. These predictions represent both an improvement on, and verification of the results published by Zhou et al. (1991).

Mode coupling and the associated redistribution of energy among the modes will not result in the large loss in transmitted signal seen in Figure 1 unless the higher-order modes have a significantly greater bottom attenuation than do the lower order mode(s). This was the situation shown in Figure 1 where the higher-order modes (2 through 8) had a bottom attenuation that was an order of magnitude larger than the lower-order mode (mode 1). This cumulative loss over the 28 km track resulted in the large loss shown in Figure 1 for frequencies near and at 630 Hz.

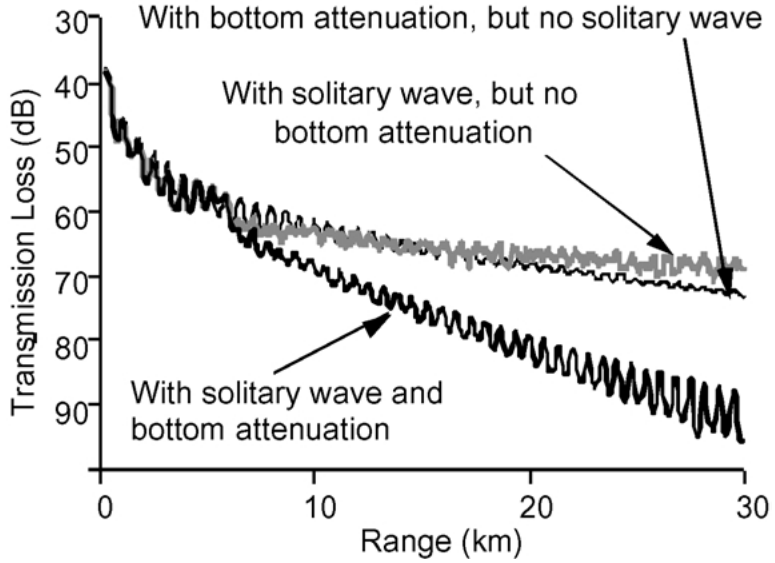

Figure 4. Mode conversion (lower to higher order modes) + higher bottom attenuation of the converted modes = high loss at the resonance frequency.

The important role that the ocean bottom has in the solitary wave resonance effect is shown in Figure 4 where Yellow Sea acoustic simulations were made (King et al., 1994) for the following three cases: (1) solitary wave present but bottom attenuation was set to zero; (2) no solitary wave was present but bottom attenuation was present; and, (3) both solitary wave and bottom attenuation were present. The presence of the solitary wave results in mode coupling and a redistribution of energy among the propagating modes. However, when no bottom attenuation is present (or if each mode has identical attenuation), the total pressure due to the redistributed modes is the same as it was before the redistribution. In fact, Figure 4 shows that the effect of bottom attenuation is more significant on signal loss than is the presence of the solitary waves. The greatest loss occurs when both solitary waves and higher attenuation are present.

In summary, at the resonant frequency (frequency at which maximum attenuation occurs) the acoustic field interacts with the solitary wave packet and acoustic mode coupling occurs; this results in mode conversions (acoustic energy is redistributed from lower-order to higher-order modes). When the converted modes have higher bottom attenuation than the original modes, high signal loss can occur at the resonance frequency. If the bottom attenuation is not significantly higher for the converted modes, then only a modest signal loss will occur. If the acoustic frequency is not at or near the resonance frequency, no appreciable loss will occur due to the acoustic field passing through the solitary wave train. It should be noted that the mode coupling and mode conversions can go from lower-order modes to higher-order modes and vice-versa. Moreover, mode conversion occurs continually

as the acoustic field passes through the environmental inhomogeneity (i.e., solitary waves) and the environmental inhomogeneity is in a medium where random fluctuations are continuously occurring. Thus, the problem is a very complex and difficult one.

2.3. Angle of acoustical propagation relative to solitary wave plane

It has been asserted that the simple relationship between the solitary wave "effective" spatial wavenumber ($K_{\text{Solitarywave}}$) and the adjacent wavenumbers (k_{Acoustic}) of the propagating acoustic modes can predict the frequency (or wavelength) where mode coupling is likely to occur (Zhou et al., 1991),

$$K_{\text{Solitarywave}} = \Delta k_{\text{Acoustic}} = \left(\frac{2\pi}{\lambda_m} - \frac{2\pi}{\lambda_n} \right), \tag{1}$$

where m and n are acoustical mode indices, and $\Delta k_{\text{Acoustic}}$ represents the difference in the acoustic wavenumbers. Energy in the acoustic wave can transfer between adjacent acoustic modes m and n when the differences in the wavenumbers of modes m and n are comparable to the "effective" horizontal spatial wavenumbers of the solitary wave.

We have used computer simulations to show that it is the "effective" horizontal component of $K_{\text{Solitarywave}}$ in Equation (1) that is important. For those simulations a solitary wave packet was modeled as a gated sine wave consisting of 6 solitary waves each with a wavelength of 235 m ($K_{\text{Solitarywave}} = 0.0267\ \text{m}^{-1}$). This is shown in Figure 5(a) where the track between source and receiver is parallel ($\theta = 0$) to the propagation direction of the solitary wave, and at angles, θ, to the propagation direction of the solitary wave. Note that the "effective" horizontal component of $K_{\text{Solitarywave}}$ in Figure 5(a) will change as θ changes, i.e., as the source-receiver track changes relative to the solitary wave direction of propagation. Figure 5(b) shows a computer simulation for a solitary wave environment similar to that used in the Yellow Sea simulations. These plots show transmission loss at a range of 28 km as a function of frequency for three different angles, θ. Note that significant signal loss occurs at two resonant frequencies for transverse angles $\theta = 0$ and $\theta = 50°$, and does not occur at all for $\theta = 30°$. At $\theta = 30°$ there are no allowable acoustic mode couplings which satisfy Equation (1). Note also that, while large signal loss is observed for both $\theta = 0$ and $\theta = 50°$, the magnitude of the losses and the resonant frequencies are different in the two cases. These results are consistent with Equation (1) and the concept of "effective" horizontal component of $K_{\text{Solitarywave}}$.

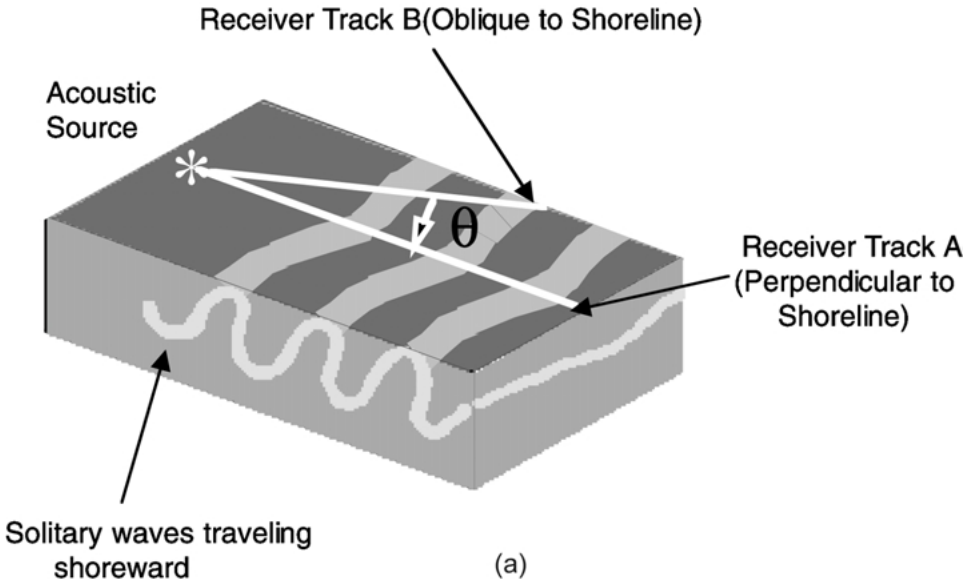

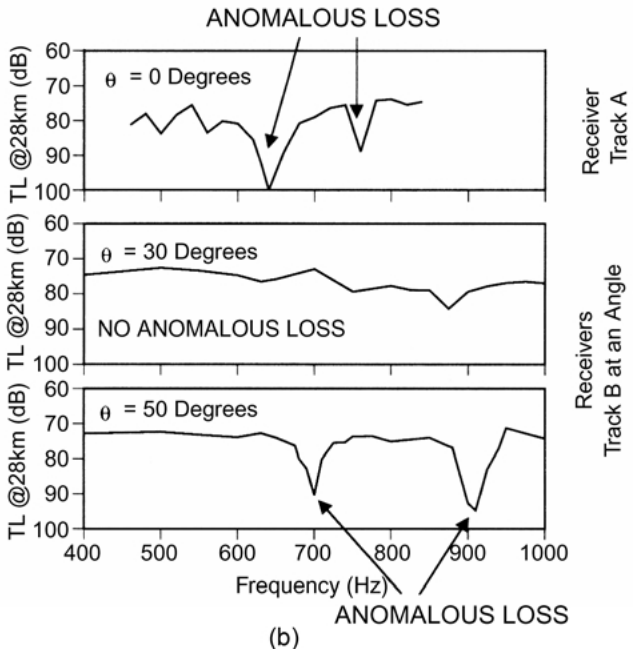

Figure 5. Acoustic computer simulations showing the effects on anomalous transmission loss (TL) as a function of angle between the solitary wave direction of propagation and the acoustic source/receiver track. The effective horizontal component of the solitary wave is $K_{\text{solitarywave}} \cos\theta$.

3. Ocean-Acoustic Modeling

To date, few coupled ocean-acoustic modeling efforts of solitary waves and their effects on the acoustical field have been undertaken.

Shang et al. (1999) performed numerical simulations of acoustical propagation using data from COPE (Coastal Probing Experiment) conducted off the Oregon coast during September–October 1995. Transmission loss calculations in the range of 50 to 1000 Hz yielded the result that for lower frequencies, $<$100 Hz, the propagation is adiabatic. For higher frequencies, $>$200 Hz, significant mode coupling takes place which results in a 5 to 10 dB loss when solitary waves are present. No strong resonant loss was found.

Finette et al. (2000) performed joint ocean-acoustic modeling in conjunction with the SWARM experiment data. The oceanographic field was separated into a perturbation type of configuration that consisted of a horizontally averaged part, an internal wave part, and a solitary wave part. The horizontally averaged part was obtained from hydrographic data, chosen along the measurement track. The internal wave part was derived from observed spectra and could be varied in time. The solitary wave component was predicted with a KdV type model which has a form of solitary wave solution that is referred to as the "Dnoidal" solution (Apel et al., 1998). The parameters for the Dnoidal solitary wave solution were derived from hydrographic observations. The approach was essentially two-dimensional in a vertical plane. A three-dimensional picture was constructed by assuming parallel two-dimensional vertical planes.

Joint ocean-acoustic modeling was performed for a source and receiver configuration 42 km apart, at frequencies of 224 and 400 Hz. A PE model was used for the acoustical calculations. Acoustical intensities were calculated at the receiver. The resulting transmission loss was qualitatively comparable to observations (Finette et al., 2000). Further work on quantitative comparisons against acoustical field measurements (involving intensity, coherence, and variability of the acoustical field) at the receiving vertical array is in progress.

The authors of this paper have undertaken an ocean-acoustic modeling effort in the Strait of Messina where there semidiurnal tidal flow over a sill generates internal bores. The internal bores propagate away from the sill and their leading edges disintegrate into solitary waves. In October 1995, NATO's SACLANT Centre tracked chosen solitary wave trains in the Strait of Messina with a Conductivity Temperature Depth (CTD) chain. We have analyzed the measurements and used them to guide a joint ocean-acoustic modeling study of solitary waves and their effects on acoustics.

The Strait of Messina oceanographic numerical simulations were performed with a two-layer reduced gravity model that was developed at the University of Hamburg by Brand et al. (1997). The model is weakly nonhydrostatic and is formulated in terms of transports and layer thickness equations. The channel width enters into the transport formalism together with the layer thickness and velocity.

The topography is in the lower layer. A constant density is prescribed in each layer. The model is essentially two-dimensional with grid points in the horizontal and layers in the vertical.

The model is forced by imposing from data a semidiurnal tidal displacement at the two open boundaries. The imposed amplitudes are 17 and 10 cm for the Ionian and Tyrrhenian Seas with a phase difference of 174 degrees. The nearly opposite phase difference (amplitudes are small) drive the resulting large tidal currents, up to 2.8 m/s. The large tidal currents depress the thermocline and generate internal bores that propagate away from the sill. Under favorable conditions the nonlinear terms cause the leading edge of the bore to steepen. Then, through amplitude and frequency dispersion, the bore disintegrates into solitary waves.

The smoothed Strait of Messina topography that was used in the model is shown in Figure 6 together with the channel width. The Ionian Sea is on the southern side and the Tyrrhenian Sea on the northern side. The sill in the strait rises to within 80 m of the surface. The computational domain extends from -30 km to 22 km with a horizontal resolution of 100 m. The time step used in the simulations was 1 second, with interface and bottom friction parameters of 0.001 and 0.01. The base horizontal viscosity was 10 m^2/s.

The prognostic variables of the model are the transports and surface elevations of the two layers. The parameters that characterized the water stratification were the initial interface (or upper layer) depth and the prescribed densities in each layer. A schematic of the variables and parameters is shown in Figure 6(c). The equations are described in Appendix A.

The acoustical transmission loss calculations were performed using the same acoustic model, FEPE, that was briefly discussed in Section 2. FEPE uses energy conservation techniques and is capable of propagating acoustic energy at nearly 90 degrees to the horizontal. The model has been benchmarked (Collins, 1990; Chin-Bing et al., 1993) and been shown to be capable of very accurate acoustic simulations.

4. Strait of Messina Data Set and Analysis

In October 1995 a survey of the Atlantic Ionian Stream was conducted in the Strait of Sicily. This survey, referred to as AIS-95 (Atlantic Ionian Stream-95), was part of a series of sea trials that involved rapid assessment of the mesoscale field (Robinson et al., 1999). At the end of this sea trial, on October 24 and 25, solitary wave trains were tracked in the Strait of Messina with a towed CTD chain. The chain had 83 sensors attached on a 270 m cable. The accuracies of the sensors were 0.01 K for temperature and 0.02 ppt for salinity. The resultant horizontal and vertical resolution was 5 and 2.5 m at a ship speed of 2.5 m/s (Sellschopp, 1997). Ocean current data were also measured with the ship's 75 kHz acoustic-Doppler-

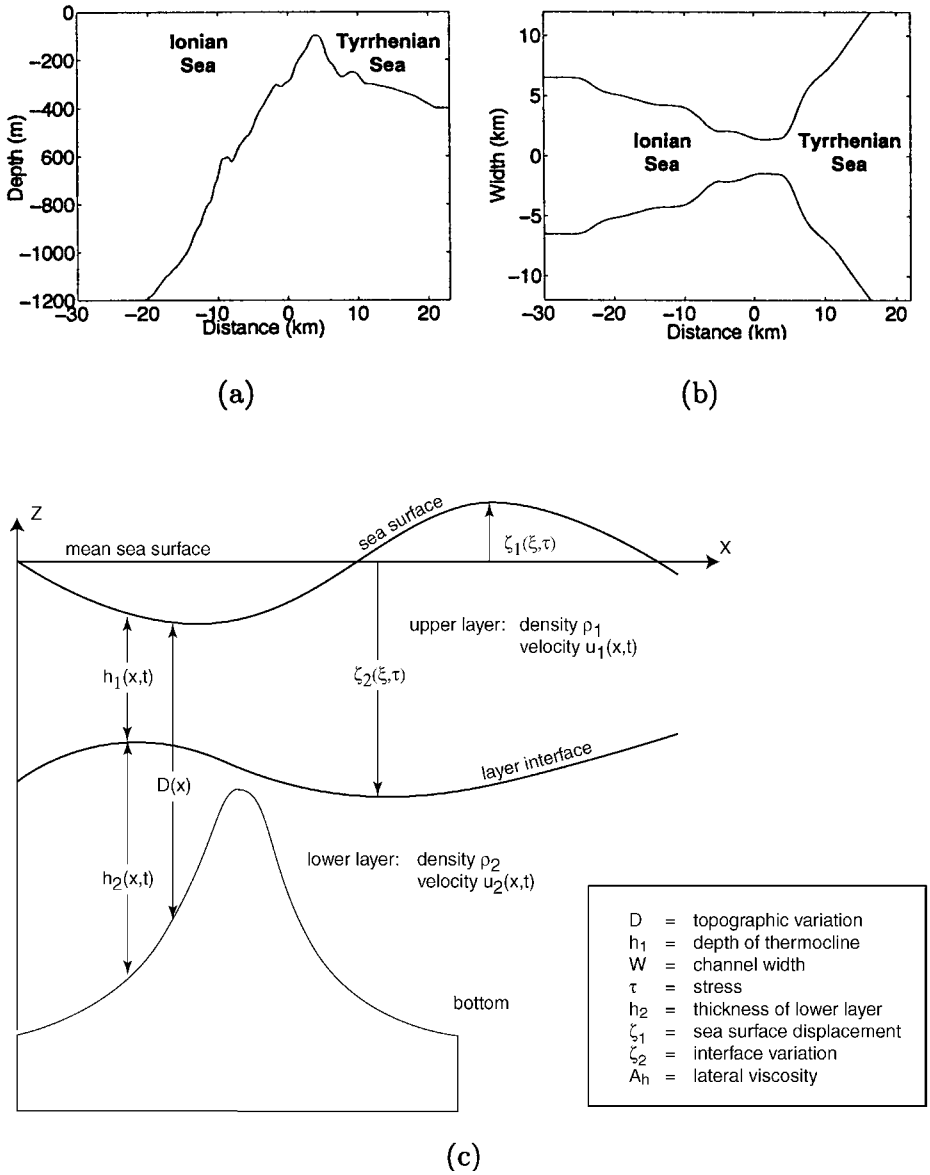

Figure 6. (a) Strait of Messina topography, (b) Strait of Messina channel width, and (c) two-layer model geometry and parameters.

current-profiler (ADCP). It was configured into 8 m vertical bins with a horizontal resolution of about 150 m at a ship speed of 2.5 m/s (Brand et al., 1999).

The data were collected by crossing selected solitary wave trains several times on the Ionian and Tyrrhenian sides of the sill in the Strait of Messina. The meas-

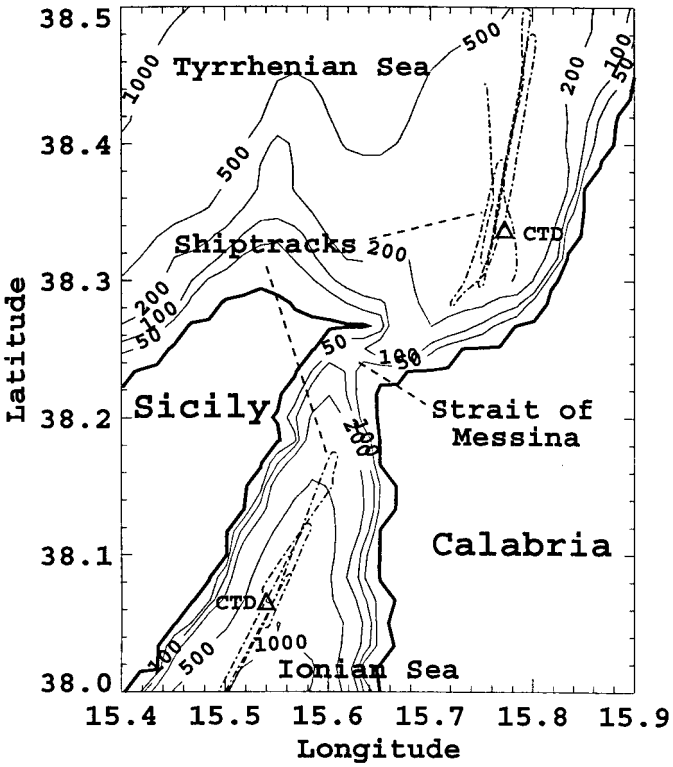

Figure 7. Location of measurements in Strait of Messina.

urements were conducted at a ship speed from 2 to 3 m/s with the solitary wave trains propagating at around 1 m/s (Brand et al., 1999).

A southward propagating solitary wave train, in the Ionian Sea, was tracked by crossing through it back and forth 5 times, Figure 7. Another northward propagating train, in the Tyrrhenian Sea, was crossed four times by the same approach. The measurements contained a Doppler shift caused by the motion of the ship relative to the propagating solitary wave trains. The shift was removed through a correction procedure.

The density distributions that were measured at the CTD stations (shown as triangles in Figure 7) on both sides of the strait are shown in Figure 8(a). At the southern station there is a well developed mixed layer of 40 m and a strong seasonal thermocline extending to about 100 m depth. On the northern side, there is a seasonal thermocline, down to about 60 m, without a mixed layer on top. The densities obtained by averaging the CTD chain data (over the track) are also shown in Figure 8(a). On the Ionian side the averaged σ_t is smoother than the CTD station observations with less sharp boundaries of the seasonal thermocline, including the absence of a feature at around 100 m that is observed at the CTD station. The densities obtained by averaging the CTD chain data on the northern

side (Tyrrhenian Sea), Figure 7, show a shallower thermocline than on the Ionian side. Towards the bottom of the thermocline, around 60 m, the averaged CTD chain data is smoother and less dense than the measurements at the CTD station, similar to the southern side. The densities in the Tyrrhenian Sea indicate heavier water than those in the Ionian Sea only in the upper 150 m.

Interpretation of cruise data (Brand et al., 1997) showed that an anomalous intrusion of Atlantic water was present in the Strait of Messina during the cruise. This caused the surface water on the Ionian side of the strait to be lighter. Subsequently during northward tidal flow the lighter water was transported into the surface region on the Tyrrhenian side. During southward tidal motion, the surface waters of the Tyrrhenian Sea spread as a subsurface jet into the Ionian Sea at a depth of 100 m. This is the opposite of the conditions that normally occur in the Strait of Messina region. Evidence for the anomalous conditions has also been found through water mass analysis of the cruise data by Warn-Varnas et al. (1999).

An EOF (Empirical Orthogonal Functions) analysis of the CTD chain data was performed. The mean states were defined by averaging the CTD chain data (as discussed previously) and are shown in Figure 8(a). As shown in Figure 8(b) on the Ionian side, the first EOF accounts for 83% of the variance, the second EOF for 7% and the third for 3%. The first EOF shows a maximum variance at 70 m, (Figure 8(b)). This corresponds to the center of the seasonal thermocline.

On the Tyrrhenian side the EOF analysis yields variances of 79%, 9%, and 4% for the first, second, and third EOF's. The variance of the first EOF peaks at 45 m and corresponds to the middle of the seasonal thermocline.

5. Parameter Space Studies

5.1. IONIAN SEA

We have conducted numerical simulations, with the University of Hamburg two layer model, of the cruise conditions encountered during the October 1995 survey in the Strait of Messina. Initially, the layer densities and upper layer thickness were set to values determined by the EOF analysis of the hydrographic observations.

The numerical simulations were begun by setting the model parameters for the Ionian Sea side of the strait. At first the upper layer thickness was set to be 70 m and corresponded to the center (or maximum variance) of the thermocline as derived from the EOF analysis, Figure 8(b). The densities of the layers were calculated from the CTD observations, Figure 8(a), by integrating the measured values over the chosen layer thickness. This yielded the values listed for case S2v0 in Table I where the first column lists an identification number; the second, h_1, is the initial upper layer depth; Columns 3 and 4 are the prescribed densities for the upper and lower layer, respectively. The last column is the lateral viscosity. First we attempted to match the simulated phase speed of the first solitary wave

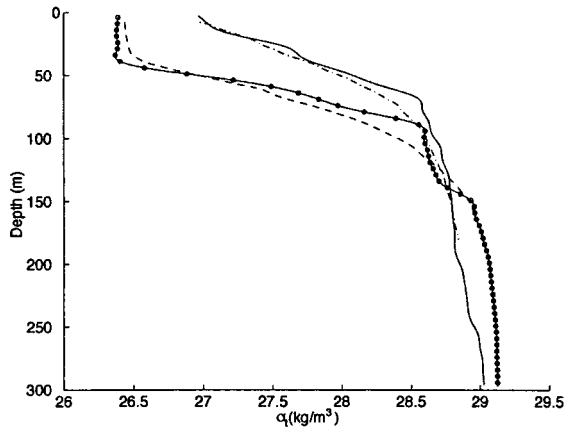

(a)

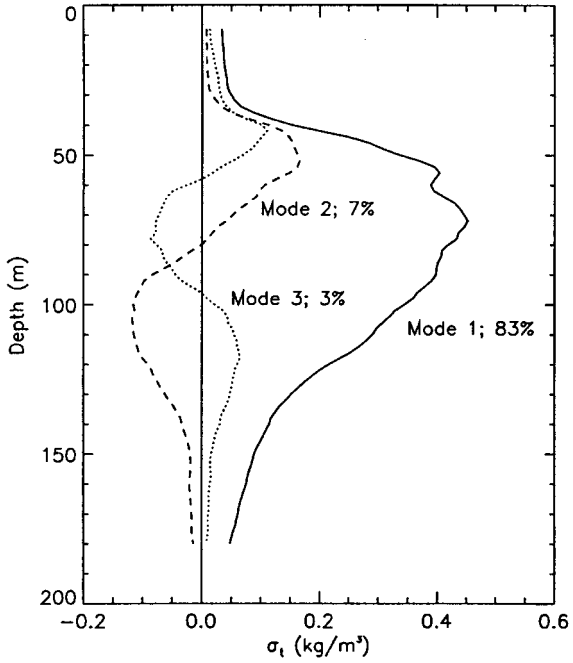

(b)

Figure 8. (a) Measured σ_t profiles in the Strait of Messina. Location of measurements are as follows: line-circle CTD station in Ionian Sea, dashed line mean profile of CTD chain data in Ionian Sea, solid line CTD station in Tyrrhenian Sea, and dot dash is the mean profile of CTD chain data in the Tyrrhenian Sea. (b) 1, 2, and 3 empirical orthogonal functions for the Ionian Sea.

with the observations. As mentioned, the parameters were set to the case S2v0 and a numerical solitary wave simulation was obtained over a semi-diurnal tidal period. For simulation analysis purposes eleven points were placed, on the peaks and troughs, at the beginning of the solitary wave train (see Figure 9), as defined by the thermocline displacement or interface deviation of the two layer model. They were located at the peaks and troughs. A phase speed of 1.52 m/s was obtained for the first solitary wave, (through a straight line fit of locations in space and time), Table II. The data indicate a phase speed around 1.3 m/s, Figure 10(a). Since the chosen parameters yield a phase speed that is too high, we performed simulations with smaller upper layer initial thicknesses. Initial thickness values of 50, 45, and 40 m were tried (see Table II). The corresponding phase speeds decreased progressively and had values of 1.29, 1.20 and 1.06 m/s. The 1.20 m/s speed was obtained with an initial upper layer thickness of 45 m, case S3kv0 in Table I, and yielded the closest agreement with data in terms of amplitude and wavelength. We considered the first three depressions of the solitary wave train represented in Figure 9. The depressions lie between the points 1, 3, 5, and 7. The distances between the points define the wavelengths of the depressions. The amplitudes are defined as the vertical distances (or projections on the z axis) between peaks and troughs. This involves the z axis span of points (1,2), (3,4) and (5,6). Table III lists the results for case S3kv0 (45 m) at a distance of 20 km from the sill. This distance is chosen because at 20 km the first three solitary waves have evolved from the internal bore in the data and simulations. The 45 m case (S3kv0) has wavelengths of 1700 m, 1400 m, and 1100 m for the first, second, and third depressions. The data have values of 1600 m, 1100 m, and 900 m. The simulated depression wavelengths are in the range of the measurements, within a few hundred meters. The data show amplitudes of 30 m, 16 m and 12 m for the 1, 2 and 3 depressions. The simulation yields amplitudes of 30 m, 22 m and 16 m and is the closest analogue to the data (in terms of amplitude, wavelength, and phase speed) among the simulations with the parameters shown in Table I.

The effect of the lateral viscosity, A_h, on the simulation results was considered. The magnitude of the lateral viscosity was varied from 10 m^2/s to 5 m^2/s, Table I. The 10 m^2/s value was used by Brand et al. (1997) in their Strait of Messina simulations. At 20 km from the sill the wavelengths obtained for the first 3 depressions with the 5 m^2/s value were the same as those using 10 m^2/s. The phase velocities of the first solitary wave increased by 0.05 m/s for each case, or about 4% when using 5 m^2/s. The amplitudes of the first, second, and third depressions increased by a few meters. The wavelengths of the depressions tended to be the same as the viscosity changes.

We have analyzed the progressive evolution of the measured and modelled solitary wave trains. The analysis was conducted by placing points on the peaks and troughs of the depressions in the solitary wave train. Seven points were placed on successive peaks and troughs of the measured solitary wave trains and eleven on the modelled trains. More points were placed on the simulated solitary wave

TABLE I
Parameter variations.

#	h_1 (m)	ρ_1 (Kg/m^3)	ρ_2 (Kg/m^3)	A_h (m^2/s)
S2v0	70	1026.7	1029.0	10
S2v5	70	1026.7	1029.0	5
S2pv5	70	1025.9	1029.0	5
S2mv5	70	1027.6	1029.0	5
S3v0	40	1026.4	1029.0	10
S3v5	40	1026.4	1029.0	5
S3iv5	45	1026.4	1029.0	5
S3kv0	45	1026.4	1029.0	10
S4v0	50	1026.4	1029.0	10
S4v5	50	1026.4	1029.0	5

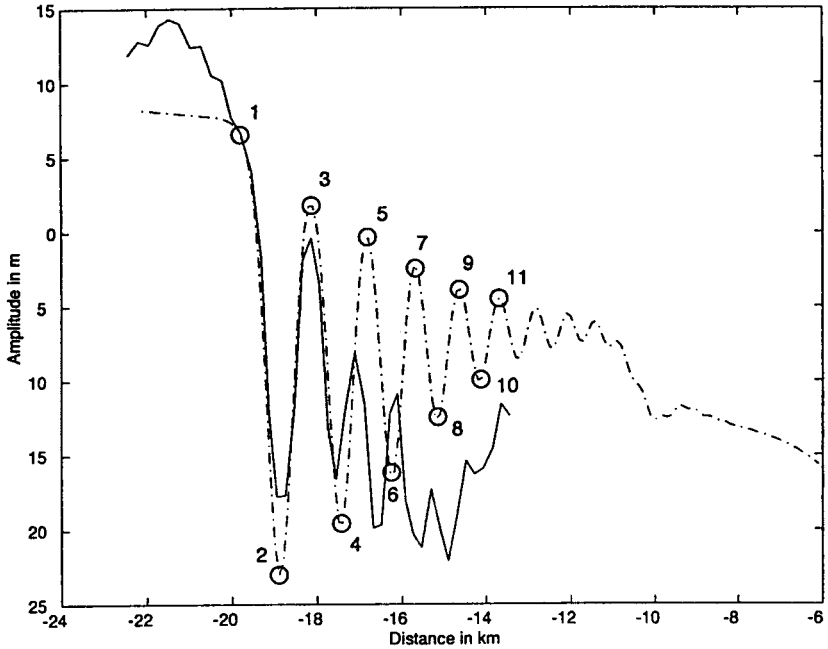

Figure 9. Measured and simulated thermocline displacement when the solitary wave train is at 20 km. Distance are from sill. Data are indicated by the solid line and the simulation by the dot dash line. The numbered circles represent points placed on the simulated peaks and troughs for tracking of solitary wave structure.

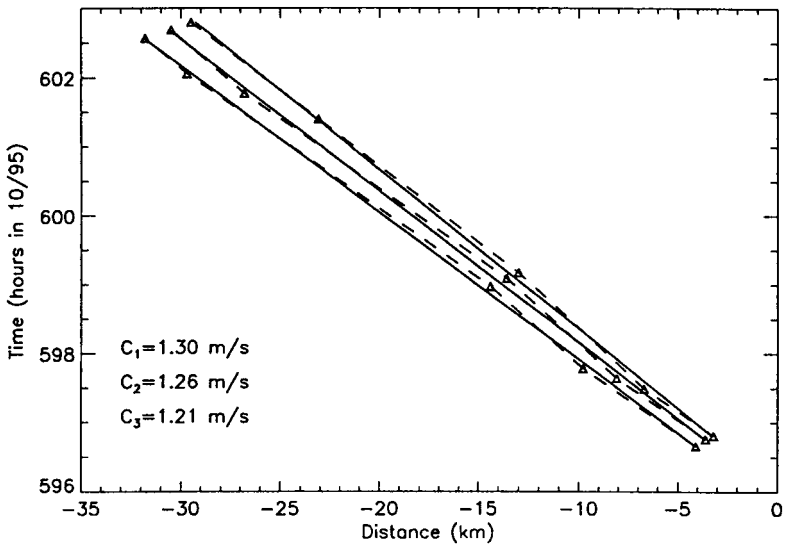

(a)

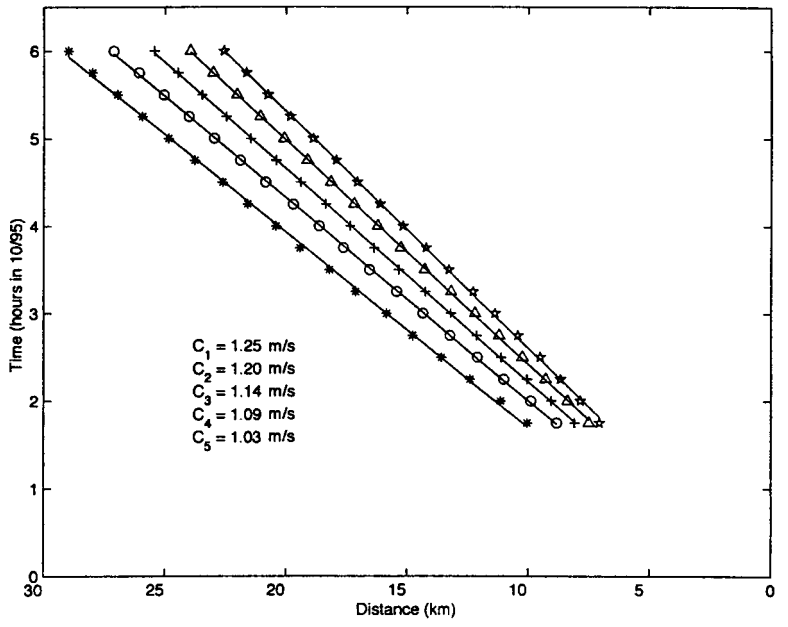

(b)

Figure 10. (a) Evolution of the measured first three depressions in space and time. The corresponding phase speeds are listed. (b) Evolution of the simulated first five depressions in space and time for case S3kv0. The corresponding phase speeds are listed.

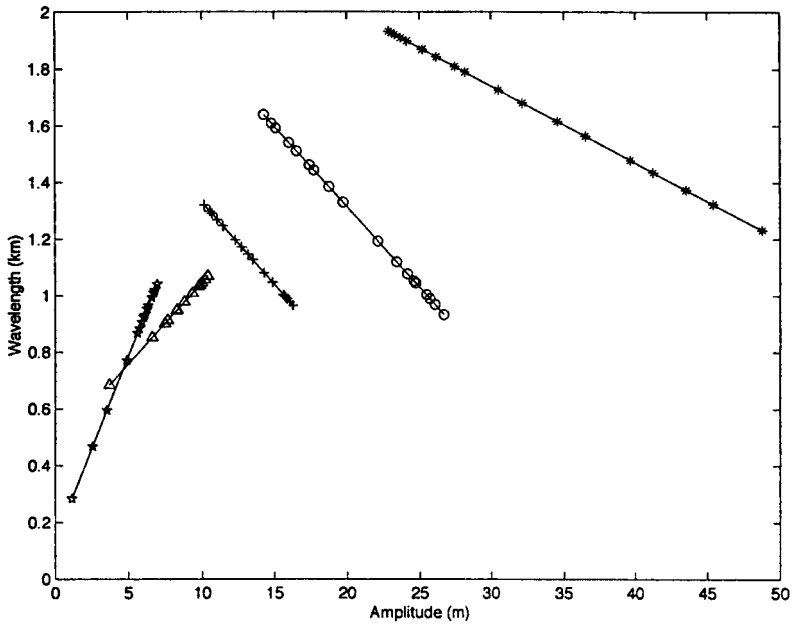

(c)

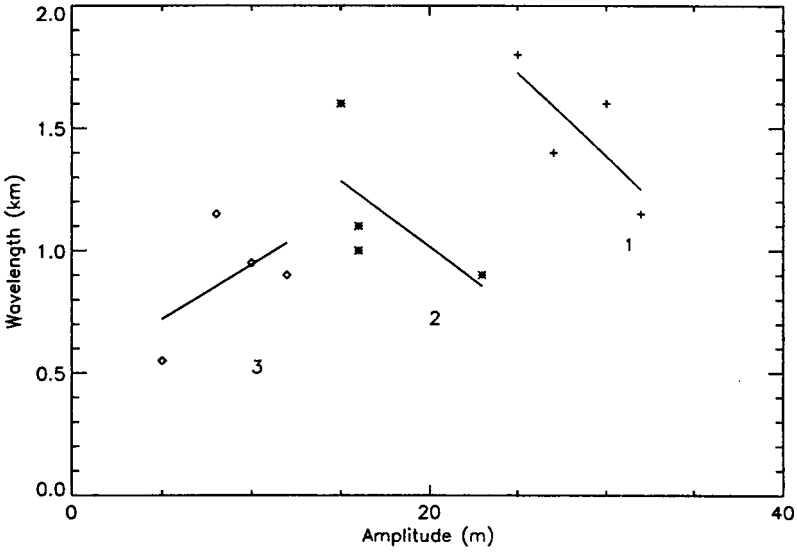

(d)

Figure 10. (c) Dispersion diagram of simulated amplitudes and wavelengths for the first five depressions. The labelling of the depressions is as follows: 1-asterisk, 2-circle, 3-plus, 4-triangle, and 5-star. (d) Dispersion diagram of measured amplitudes and wavelengths for the first three depressions. The labelling of the depressions is as follows: 1-plus, 2-asterisk, and 3-square.

TABLE II

Phase speeds of first solitary wave.

#	C_1 (m/s)
S2v0 (70 m)	1.52
S4v0 (50 m)	1.29
S3kv0 (45 m)	1.20
S3v0 (40 m)	1.06

TABLE III

Measured and simulated characteristics.

	Simulation	Data
Wavelengths of 1, 2,	1700 m	1600 m
and 3 depression	1400 m	1100 m
	1100 m	900 m
Amplitudes of 1, 2,	30 m	30 m
and 3 depression	22 m	16 m
	16 m	12 m

trains because they were well defined. The placement is illustrated in Figure 9. The displacement of the points was tracked in time and space.

In Figure 10(a) we show the progression of points placed on the peaks preceding the depressions in the measured solitary wave trains. Three curves are shown because only the first three depressions are resolvable in the data. The data points are indicated by triangles and are connected by dashed lines. On each line only five triangles appear because the solitary wave train was tracked five times. The solid lines are straight line fits to the data points. From left to right the first line represents the point preceding the first depression. Then the second and third depressions are tracked correspondingly. The phase speeds obtained from straight line fits are 1.3 m/s, 1.26 m/s, and 1.21 m/s for the first, second, and third depressions with a relative error of 4%.

For case S3kv0 (our best tuned simulation) in Table I we conducted an analogous analysis by placing eleven points on the peaks and troughs of the solitary wave train. The simulated interface by the model is well defined in space and time. As a result we were able to track the first five depressions in the train. The availability of the model results at chosen intervals enabled the tracking to be performed at 18 intervals as indicated by the points in Figure 10(b). The progressive phase speeds of

the straight line fitted depressions ranged from 1.25 m/s to 1.03 m/s with standard deviations of 0.032 to 0.024, respectively.

From the location of the points, placed on the solitary wave train, we have computed the wavelengths and amplitudes of the depressions as they propagate. The amplitudes were determined by projecting point differences on the vertical axis and the wavelengths were computed from differences along the horizontal axis. The resulting dispersion curves are shown in Figure 10(c).

The points on the curves represent the 18 samples of the solitary wave trains along the horizontal propagation axis. The solid lines are the straight line fits to the samples. From the upper right hand corner to the lower left hand corner the curves represent the first through the fifth depressions. For the first, second, and third depression the initial amplitude is large and the wavelength is small. As the depressions propagate the amplitudes decrease and the wavelengths increase. This is the amplitude versus wavelength behavior of a solitary wave in the Strait of Messina as it propagates and undergoes radial spreading, diffraction, depth change and dissipation. The solitary wave width increases as its amplitude decreases. The trend reverses for the fourth (triangle) and fifth (star) depression. These depressions start out as waves of small amplitude and wavelength. They are still in the evolving stage into solitary waves. At this stage, the wavelength and amplitude increases. Once they evolve, the wavelength increases and the amplitude decreases.

In the measured solitary wave trains, we tracked the first three depressions. The others were not distinguishable. Seven points were placed on the measured solitary wave train. We considered four trackings of the solitary wave train with four samples for each of the three depressions. The extracted wavelength versus amplitude dispersion diagram is shown in Figure 10(d). The first three depressions that were analyzed are marked 1, 2, and 3 with the corresponding data points (at which the amplitude and wavelength were determined) marked by plus, asterisk, and square. Each depression was tracked in four consecutive solitary wave trains indicated by four data points. The solid lines are regression fits to the data points. The normalized root mean square (rms) values vary from 0.1 to 0.2, with correlations of 0.53 to 0.76. For the first and second depressions the amplitudes decrease and wavelengths increase as the depressions propagate. This trend agrees with the model results and is the expected dispersion behavior. The initial amplitude value of the third depression is around 5 meters. As a result the trend of the slope is changed, resulting in a decreasing amplitude and wavelength. The low 5 meter value could be due to the presence of an extraneous feature or to the depression being still in the growing stage.

The model results indicate an increasing slope from the first to second depression. The data show a slight decrease for the slope of the second depression relative to the first (both slopes are increasing). However, the data points are few and they scatter about the regression line, Figure 10(d).

For the first depression the wavelength versus amplitude slope is larger in the measured dispersion than in the model simulation. For the second depression the

trend reverses and the slope of the wavelength versus amplitude becomes larger in the simulation results. For the third depression, the wavelength versus amplitude slope in the model simulation disagrees with the fitted real data trend. The dispersion of the data is, however, hard to estimate because of the larger scatter of the measured values.

We compared the interface deviation of case S3kv0 (45 m) with the measured thermocline deviation in Figure 9. The first and second depressions marked by points (1,3) and (3,5) show phase agreement. The amplitude of the second depression is, however, larger in the simulation and the rise from the second trough to the peak is higher than in the data. As a result the phase agreement is lost and the simulated third depression is in opposite phase.

The measured solitary waves are superposed on a background with a decreasing mean height as one proceeds in the horizontal direction. The corresponding mean of the model simulation is higher than the one in the data. The mean backgrounds contain the signatures of the internal bores that have a depression type of shape after generation at the sill. Variation of the parameters can yield simulated background means at 20 km that are analogous to the data but with larger amplitude and wavelength differences than the previous case. The opposite phase problem, however, remains beyond the first two depressions. This suggests missing physics from the two layer model, since no oceanic features besides solitary waves are observed at 20 km in the data.

6. Comparisons of Simulated Density Fields with Measurements

6.1. IONIAN SEA

On the Ionian side of the strait, measurements of the solitary wave trains were conducted at around 10, 15, 20, 35, and 38 km from the sill. Model simulations were available for comparison at 10, 15 and 20 km because the model domain extended to about 30 km on the Ionian side of the strait. Near 20 km the measured solitary wave train is well evolved and behaves according to expectation in terms of amplitude and wavelength characteristics, by exhibiting decreasing amplitudes and wavelengths in the train. We therefore chose the 20 km location for the initial comparison of modelled solitary waves train characteristics with data.

Figure 11(a) shows the measured sigma-theta density distribution in the upper ocean, over the extent of the CTD chain reach. The data were lowpass filtered with a Butterworth filter. Isopycnal contours are superposed on the graph and illustrate the solitary wave train structure. The solitary waves propagate in the horizontal and displace the isopycnal throughout the water column. The isopycnal displacements have a vertical structure that can be described through a vertical structure function. As the upper boundary is approached,the isopycnal displacements decrease and go to zero at the boundary where the structure function is zero. The initial solitary

waves in the train has the largest isopycnal depression (from equilibrium) and wavelength. The second and third depressions decrease in amplitude, progressively, and tend to have smaller wavelengths. In the center of the thermocline, around 70 m, the mean of the isopycnals tends to outline an internal bore (depression type of shape) on whose leading edge the solitary waves are superposed. Further down the thermocline, around 120 m, the background depression shape becomes more flat on its tail end.

At about −10 to −11 km from the sill, there is a signature of up and down lifting in the 28.0 and 28.4 isopycnals in the span from 80 to 130 m. This bifurcation type of feature is visible in other solitary wave train measurements at the back end of the propagating internal bore, suggesting that it is part of the dynamics. The bifurcation could be due to a mode 2 wave. The corresponding model simulations are shown in Figure 11(b). The density distribution was constructed using the relation,

$$\rho = \rho_0(z) + \zeta(x,t)\frac{\partial \rho_0(z)}{\partial z}, \tag{2}$$

where $\rho_0(z)$ is a reference density and $\zeta(x,t)$ is the interface displacement. This result was obtained using a perturbation expansion of the transport equation for density (or sound speed) in conjunction with a layer model formalism that has surface deviations. The derivation considers a time change in density transport (or sound speed) in presence of a layer whose interface is ζ. The isopycnals are displaced down and up during the passage of solitary waves. In the derivation it is assumed that the interface displacement, $\zeta(x,t)$, is the same throughout the water column. This assumption is mitigated by the structure of the vertical derivative of the reference density $\partial\rho/\partial z$ that peaks in the thermocline and tends towards zero away from it (in a first mode type of behavior). The approach is outlined in Essen (1976).

We considered ways to improve the derivation based on Essen's (1976) work by introducing a vertical structure function (Apel, 2001). The vertical structure function, $W(z)$, appears as $\zeta(x,t)W(z)\partial\rho_0(z)/\partial z$ in Equation (2). In this case, the vertical structure function is related to the first oceanographic vertical normal mode as obtained from the Sturm-Liouville or Taylor-Goldstein equation. This eigenfunction reaches a peak in the thermocline or at the two-layer model interface. Away from the peak it decreases to zero as the upper and lower boundaries are approached. The derivative undergoes a rapid decrease away from the thermocline region and reaches small values at the outskirts. As a result, the contribution of the structure function to the reconstruction has a negligible effect.

Just as in the case of the measurements, the initial solitary wave in the train has the largest isopycnal depression and wavelength. The subsequent depression amplitudes and wavelengths are smaller. Eventually they became very small and insignificant. In all, about five to six depressions are noticeable as having defined shape and appreciable amplitude (the rest are smaller). In the data the 26.9 through 28.4 give units isopycnals show five depressions. They are located just below the

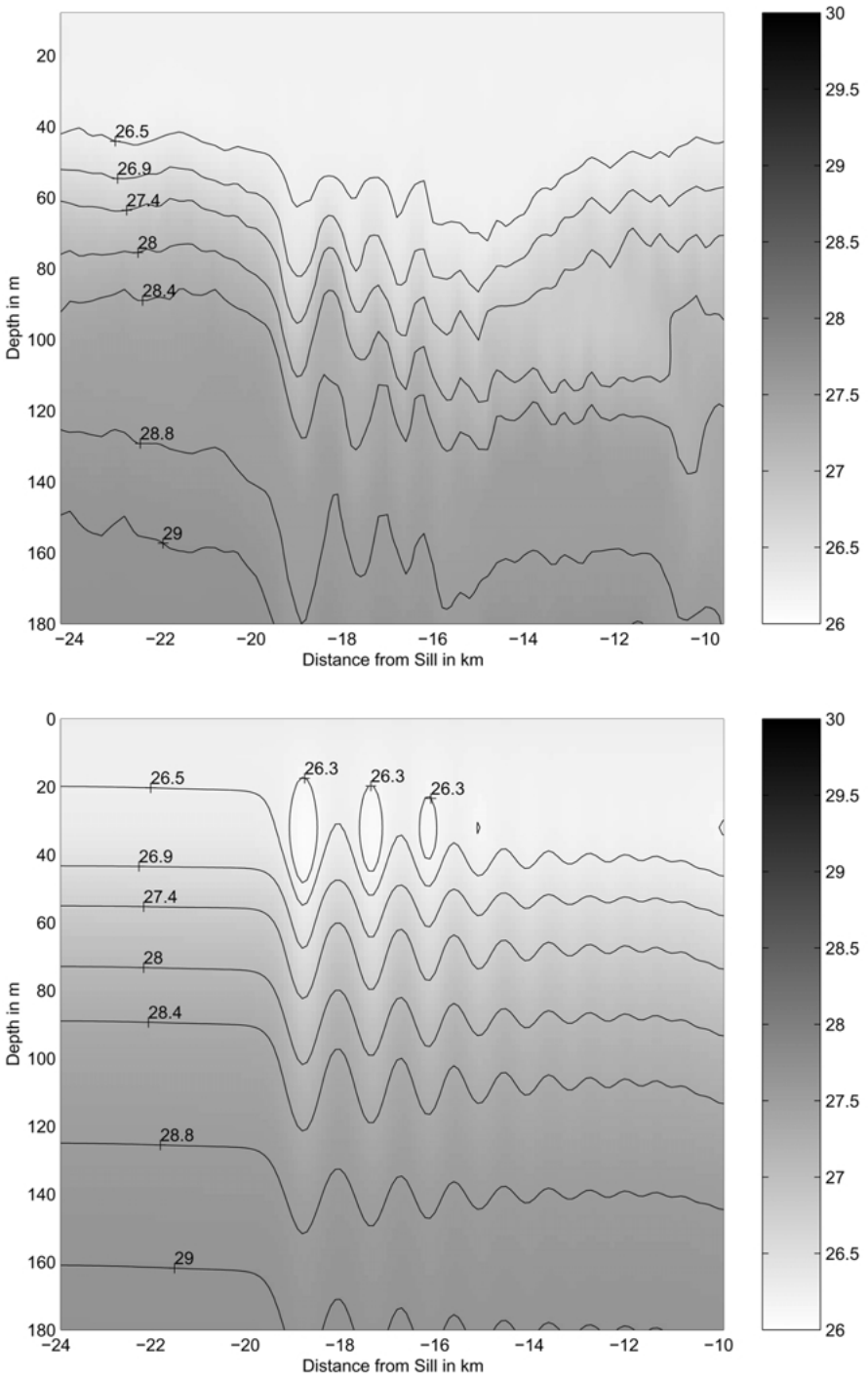

Figure 11. (a) Measured Ionian Sea sigma-theta density distribution at 20 km from the sill. (b) Simulated Ionian Sea sigma-theta density distribution at 20 km from the sill.

mixed layer and are well defined around 70 m, where the center of the thermocline is. The depression shaped internal bore signature is not visible in the background of the model simulations. The mean background is flat except for a small dip around −10 km. This dip is part of an internal bore depression formed at the sill by the semidiurnal tide. The uplifting of the 28 isopycnal and the downlifting of the 28.4 isopycnal seen in the data near 10 km does not occur in the simulation. The two-layer model is incapable of modeling such a feature.

The 26.5 units isopycnal tracks the stratification just below the mixed layer. Above the 26.5 isopycnal, there is a 26.3 closed contour. The closed contours are an artifact of the construction, for a case where the interface displacement is felt throughout the water column with a modulation of the vertical derivative of the reference density that peaks in the thermcoline and decreases towards zero away from it. The closed core contours occur at the bottom of the mixed layer in a thin pycnocline type of region.

There is some vertical shift in the modelled isopycnal locations relative to the data. The shift is an artifact of the field reconstruction using the perturbation approach. It is introduced through the background stratification and its derivative. The effects of the internal bore and solitary waves are simulated by the interface deviation of the two layer model and the measured background stratification. The measured background stratification (at the CTD station and with the CTD chain) does not reflect all of the semidiurnal tidal effects, in terms of isopycnal depression and recovery over the semidiurnal tidal period.

The availability of CTD chain measurements of the solitary wave trains suggest a quantitative comparison with the modelled solitary wave sigma-theta density fields. We adapted the statistical validation measures of root mean square error (rmse) defined as:

$$\text{rmse} = \left\langle \left(\frac{\rho_p}{\rho_o} - 1 \right)^2 \right\rangle^{1/2} \tag{3}$$

where ρ_p is the model predicted density, ρ_o is the measured density, and the angle brackets denote averaging over a specified spatial area. In the subsequent analysis, the averaging is performed over depth at each horizontal location. Here the measured density, ρ_0, is defined as the measured density distribution versus depth at the CTD stations and consists of CTD chain averages (in the upper 180 m) combined with CTD station measurements below that.

Figure 12 shows the rmse values of the prediction as a function of horizontal distance superposed on the measured isopycnals. Before the first depression the background rmse is around 0.14. This is a bias of sigma-theta reconstruction involving the background density that is derived from the CTD station and chain measurements. For the first depression the rmse is low. It starts rising in the second depression and becomes large for the next three depressions, indicative of the phase differences discussed previously. The rmse diminishes as the background

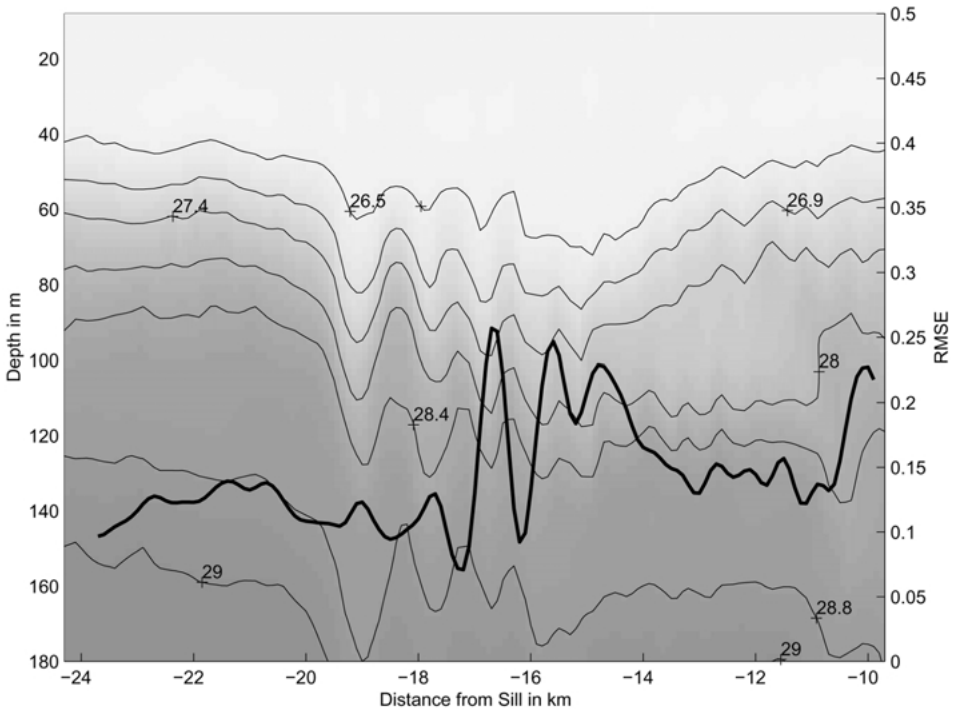

Figure 12. Relative root mean squared error (rmse), heavy solid line, of simulated to measured sigma-theta density as a function of horizontal distance. The measured sigma-theta field is superimposed.

is approached and then starts rising again in the bifurcation region around −11 km from the sill.

7. Potential Energy Distribution

7.1. Energy distribution

The potential and kinetic energies associated with the internal bores and solitary wave trains are of interest. Consider the vertically integrated available potential energy (APE) that is computed from a Taylor series expansion of the difference between the potential energy and its mean (Gill, 1982; Brickman et al., 1993),

$$\mathrm{APE} = \frac{1}{2}\int_{z_1}^{z_2}\left(\frac{g^2\rho'^2}{N^2}\right)dz, \tag{4}$$

where ρ' is the perturbation from the reference state, N the buoyancy frequency of the reference state and g the acceleration due to gravity.

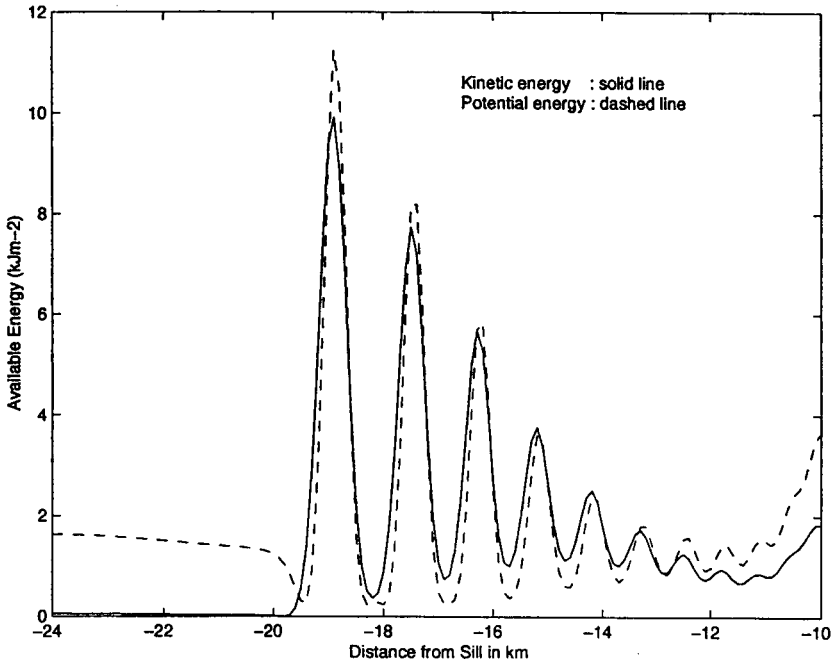

(a)

Figure 13. (a) Available upper layer potential energy and kinetic energy for a simulated solitary wave train in the Ionian Sea at 20 km from the sill.

For the reference state we use the previously defined reference state in Section 6. Using this approach, and the constructed density field using the interface deviation for the tuned parameters (case S3kv0 in Table I), we compute the available potential energy along the solitary wave tracks in the Strait of Messina.

Figure 13(a) shows the resultant available potential energy distribution, when the solitary wave train is about 20 km away from the sill in the Ionian Sea. The oscillatory signature of the solitary wave train is visible in the available potential energy distribution. As the solitary waves depress the isopycnals, the lighter fluid ends up in a denser ambient environment. The square of the deviations, relative to the ambient mean state, tracks the solitary wave amplitude distributions (Figure 11(b)). The kinetic energy integrated over the upper layer thickness (Figure 13(a)) has an analogous oscillatory distribution with comparable energy magnitudes in kJ m^{-2} (10^3 Joules per meters squared). The kinetic energy has maxima at the depressions.

The available potential energy computed from the CTD chain measurements is shown in Figure 13(b). The distribution has the oscillatory nature of the solitary wave train. The oscillatory structure of the modelled available potential energy differs from the measured characteristics. The first striking difference is the rise in background around 16 km in the data derived results relative to the Figure 11(a)

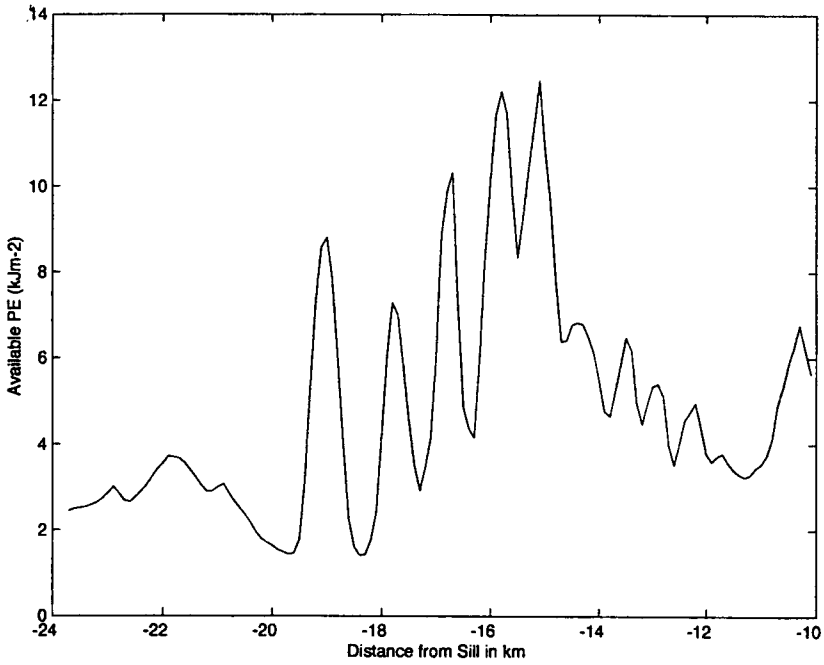

(b)

Figure 13. (b) Measured available potential energy.

simulations. The rise is due to the decrease of the mean slope from −20 to −17 km, Figure 11(a), on which the density variations are superposed. From −17 to −12 km, the mean slope raises and the available potential energy decreases, Figure 13(b).

The amplitude and phase differences previously discussed in Section 6 and shown in Figure 10 are also seen in the simulated available potential energy differences in relation to the data.

We consider the integrated available potential energy over the horizontal extent of the region shown in Figure 13(a). The measured available potential energy is 68.4 MJ/m for the domain. The corresponding modelled available potential energy is 27.9 MJ/m. This is around half of what is measured in Figure 13(b). If one considers the background (on which the solitary wave oscillations are superposed) from 16 to 10 km the contribution is around 30 MJ/m. Into this background enters the measured structure shown in Figure 11(a) from −16 km to −10 km. This structure, as previously discussed in Section 6 is not reproduced in the model results and it accounts for the large difference between modelled and measured available potential energies.

We calculate the simulated available potential energy over the sill region where the internal bores are generated. The previous definition of available potential en-

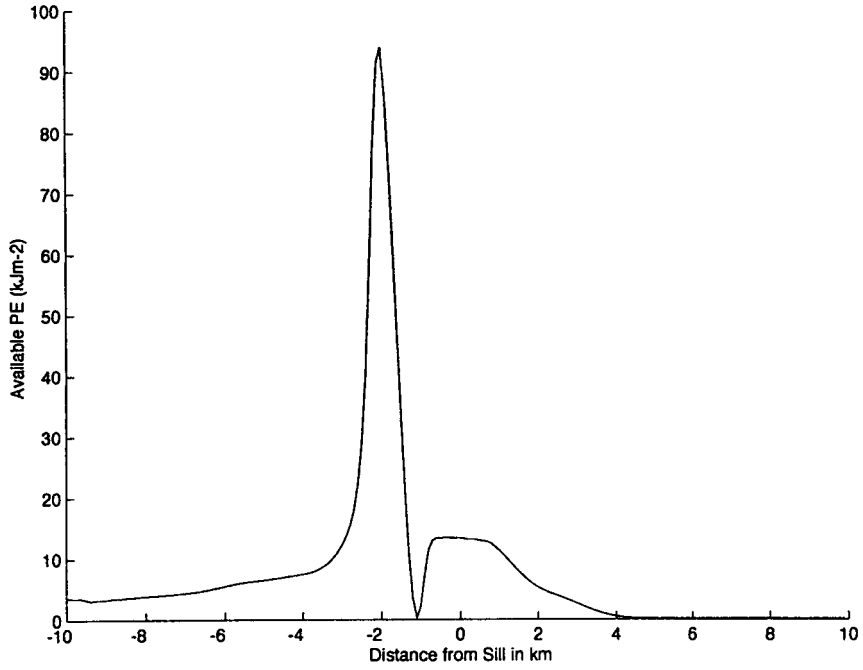

(c)

Figure 13. (c) Available potential energy for a measured solitary wave train in the Ionian Sea at the sill.

ergy, Equation (4), was used together with the same assumptions. Figure 13(c) shows the results of the calculation at the time of 0.38 tidal cycles, same as in Figure 13(b), and indicates that the available potential energy in the internal bores at generation is about an order of magnitude larger then the one contained in the solitary wave train at 20 km. The horizontally integrated energy over the domain of Figure 13(c) is 158.6 MJ/m.

8. Ocean-Acoustic Predictions and Perspectives

We have performed joint modelling studies of the oceanographic and acoustical environments. Cases from parameter space studies, in Section 5, were selected for coupling to the acoustical model (FEPE). The parameter space studies involved variations of the oceanographic parameters about the existing conditions during solitary wave generation and propagation. The sound speed was calculated by the approach outlined in Section 6 that was used for constructing sigma-theta from the interface deviation of the two-layer model. Initially, we used a background sound speed derived from the CTD station measurements in the Ionian Sea (Figure 7). The background sound speed constitutes one of the oceanographic parameters. This

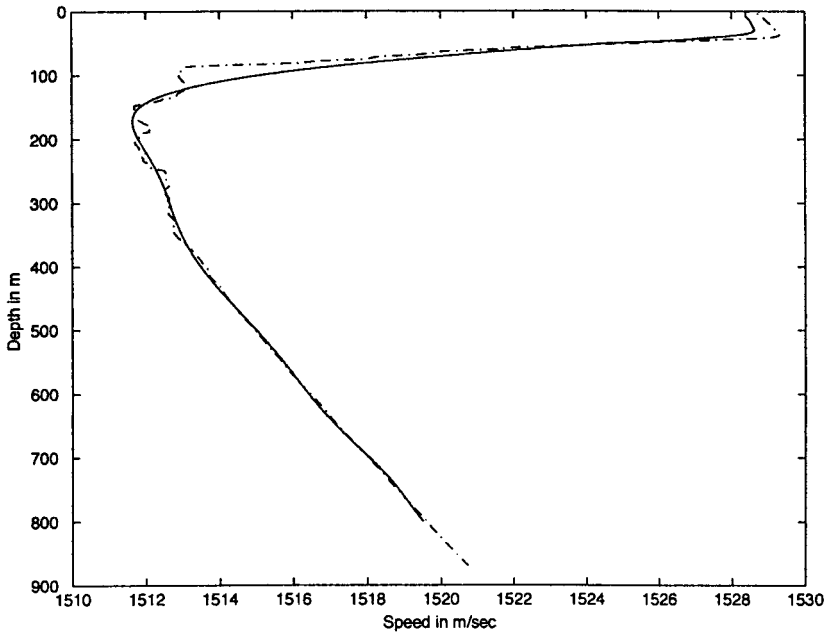

Figure 14. Sound speed measured at the Ionian Sea CTD station, dash dot line. Sound speed in the Ionian Sea derived from the CTD chain and CTD station measurements, solid line.

sound speed, as computed from the raw data, is shown by the dash-dot curve in Figure 14. The corresponding sigma-theta density distribution, at the same location, is shown in Figure 8(a). Note the existence of an oceanic feature in the vicinity of 100 meter depth.

We have generated a smoothed version of the sound speed from CTD chain data averages in the upper 180 meters. This average we merged with the CTD station measurements at depth. The CTD station data were smoothed by low pass filtering and polynomial interpolation. The result is shown in Figure 14 by the solid line. Unless otherwise stated, the smoothed version of the background sound speed is used in the perturbation reconstruction of the sound speed field.

The acoustical calculations were performed with the FEPE acoustical model. The acoustical source was located in the Ionian Sea at a range of 30 km from the sill and at a depth of 200 m. The frequency of the source was 200 Hz. The solitary wave train was at a distance of 20 km from the sill. For case S3kv0 in Table I the reconstructed sound speed is shown in Figure 15(a). The sound speed varies from 1530 m/s at the surface to 1510 m/s at the bottom. At 20 km the solitary wave train shape is visible in the sound speed structure, Figure 15(a). The depressions of the solitary wave train move the sound speed downwards, resulting in higher speed surrounded by lower ambient values that reflect the existing stratification condition before the onset of solitary waves. Also, just south of the sill is visible a sound

speed depression caused by an internal bore that has an amplitude larger than the solitary waves.

The sound speed derived from the measurements at 20 km is shown in Figure 15(b). The measurements were inserted into a background sound speed field that was derived from model simulations, because no CTD chain measurements were conducted at the sill or further away from the solitary wave location. The insertion was done by using a five point weighted average with the weights varying between data and model results. The sound speed obtained from the data has a depression type of background shape, indicative of an internal bore. The structure of the solitary wave depressions are analogous to the sigma-theta density distributions discussed previously in Section 6.

We have calculated the acoustic intensity fields with measured and predicted sound speeds. The hydrodynamic model predictions are for case S3kv0 in Table I. The parameters of this case were tuned so that the predictions matched the data as much as possible, Section 6. The acoustic intensity calculations are sensitive to the background sound speed used in its reconstruction. The calculation shown in Figure 16(a) was conducted with a sound speed reconstructed by using the background field derived from the CTD station measurement shown in Figure 14. As mentioned this background field did contain a feature at a depth of around 100 m (see Figure 8(a) and Figure 14). The acoustic intensity calculations were repeated with the smoother sound speed derived from the CTD chain and CTD station measurements, Figure 14. The resulting acoustic intensity field is shown in Figure 16(b). In the upper 200 m the large scale ray patterns in the 0 to 20 km range are smoother and have no up and down oscillations close to the surface over shallow topography in relation to Figure 16(a). This we attribute to the background sound speed's smoother structure, and the absence of a feature at 100 m causing the ray paths to bend up more, in a region of progressively shallower topography.

The acoustic intensity calculations with the measured sound speed are shown in Figure 16(c). The coarse acoustic intensity fields resemble those of Figure 16(b) which uses a predicted sound speed reconstructed with a smooth background sound speed. The fine details of the acoustic intensity fields have some differences.

We have demonstrated that acoustical intensity fields calculated with sound speeds derived from data and model predictions show agreement for some wavelengths and disagreement for others. Future research will address these issues.

9. Summary

Shallow water internal solitary waves have become a major topic of interest to oceanographers and acousticians. In this paper we have undertaken cross-disciplinary studies of solitary waves. We demonstrate that, in the presence of solitary waves, the acoustical field can interact with the solitary waves and acoustical mode coupling can occur. This results in mode conversion with acoustical

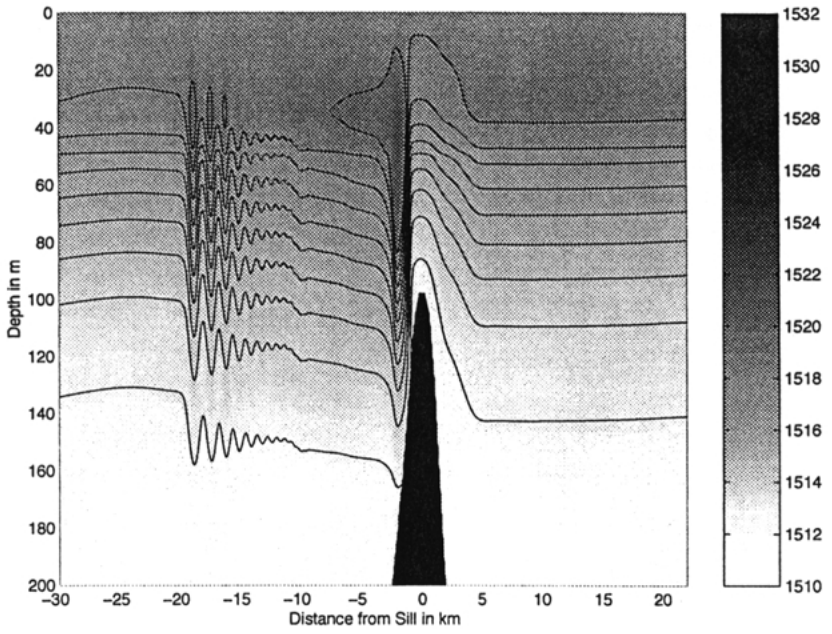

(a)

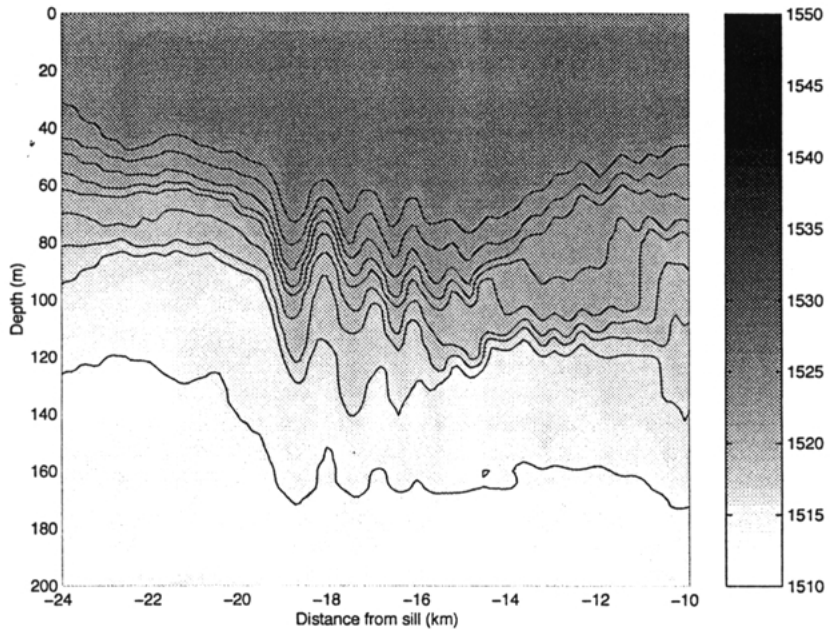

(b)

Figure 15. (a) Modelled sound speed (in m/s) in the Ionian Sea for a solitary wave train at the sill. (b) Measured sound speed (m/s) in the Ionian Sea for a solitary wave train at 20 km from the sill. The measured sound speed is imbedded into the modelled sound speed away from the data region.

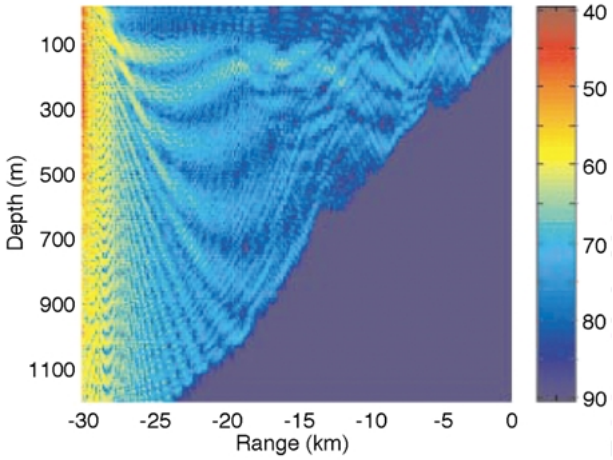

(a)

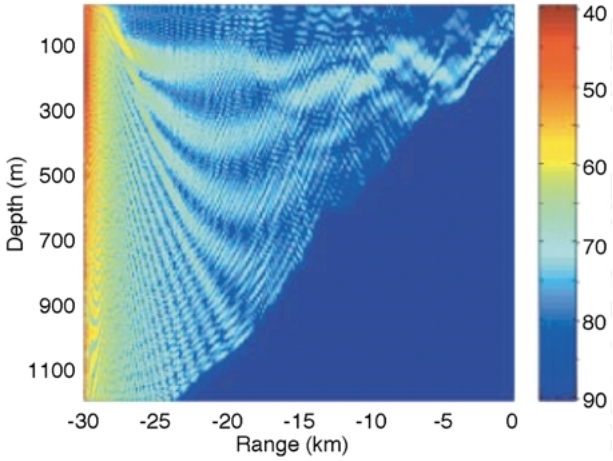

(b)

Figure 16. (a) Acoustic intensity field in a modelled environment with solitary waves and initial oceanographic parameter settings. The topography is located south of the sill. The source is at 200 m and the frequency is 200 Hz. The vertical acoustical field intensity is in dB. (b) Acoustic intensity field in a modelled environment with solitary waves and tuned oceanographic parameters.

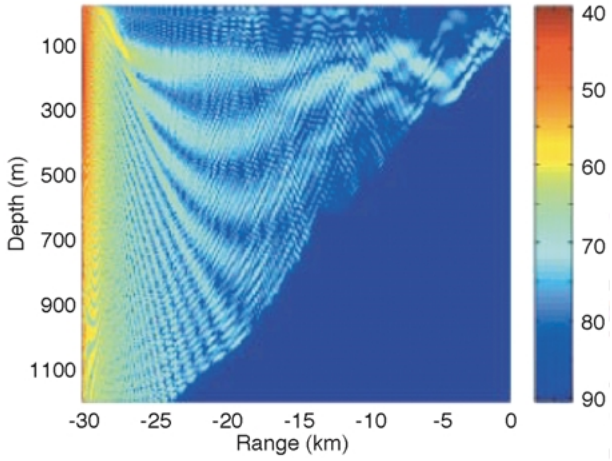

(c)

Figure 16. (c) Acoustic intensity field (dB) in the measured oceanographic environment with solitary waves.

energy being redistributed from lower to higher-order modes or vice versa. When the converted modes have higher bottom attenuation than the original modes, higher signal loss can occur. At some frequencies, called resonance frequencies, the signal loss can be large enough to cause an appreciable drop in acoustical intensity.

Anomalous loss of acoustical intensity has been studied as a function of angle between the solitary wave direction of propagation and the acoustic source receiver. A relationship (from acoustical theory) between solitary wave and acoustical wavenumbers has been applied for deriving the effective horizontal solitary wave wavenumbers oblique to the source and receiver plane of location. Transmission loss calculations established that anomalous loss of acoustical intensity can occur at oblique angles for two different frequencies.

Nonhydrostatic modelling of solitary wave generation and propagation has been performed on continental shelves and in straits. A variety of nonhydrostatic models exists in the community. Among these are layer, z-level, and sigma-coordinate models. The models are forced by barotropic semidiurnal tidal flow over sharp topographic that generates baroclinic tides in presence of stratification. A depression of the thermocline in the form of an internal bore results. The internal bore propagates and its leading edge steepens through nonlinear effects. Frequency and amplitude dispersion set in and the leading edge of the internal bore disintegrates into solitary waves.

The scientific community is beginning to undertake joint ocean-acoustic modeling. The modelling efforts have been undertaken in conjunction with various experiments that performed oceanographic, acoustical, or joint oceanographic and

acoustical measurements. Such efforts have occurred in connection with SESAME, SWARM, PRIMER, and the Strait of Messina experiments.

In the Strait of Messina there is presently a joint ocean-acoustic dynamical modelling effort in place. There the various elements of joint ocean-acoustics modelling are present and can be pursued in an unhindered manner because of the certainty that the solitary wave trains are there during the semidiurnal tidal cycle. The oceanographic and acoustical models are coupled through the derived sound speed from the nonhydrostatic model predictions. On the acoustical side various versions of the parabolic equation model are in use for acoustical intensity calculations. In the Strait of Messina we have predicted with a nonhydrostatic model the sigma-theta density distribution of solitary wave trains and have compared the predictions to CTD chain measurement. The model's sensitivity to its parameters has been studied and the parameters have been tuned for best agreement with the CTD chain measurements of solitary wave trains. The criteria for agreement were based on solitary wave phase speed, wavelength, and amplitude. The tuned numerical simulation tended to represent the structure of the first two solitary wave depressions in the train. There was phase speed, wavelength, and amplitude agreement with the best match occurring for the first depression. From the third depression on, there was disagreement. We attributed this to the unknown aspects of the problem and to missing physics in the two layer model that was used in the numerical simulation. Future work has to be done in order to sort out the situation. This will involve the comparisons of different nonhydrostatic models for chosen physical situations of solitary wave generation and propagation. The active physical processes will have to be deduced from experimental observations and theoretical work. The comparisons will lead the way to the understanding of relevant oceanographic processes and their incorporation into models.

Available potential energy calculations with predicted and measured density fields were performed. The available potential energy distributions tracked the oscillatory solitary wave behavior. The calculated kinetic energy behavior had an analogous oscillatory behavior, with comparable energy magnitudes. Calculations over the sill region yielded available potential energy levels that were an order of magnitude larger than those over solitary wave train region.

Comparisons of predicted and measured available potential energies showed the previously discussed agreements and disagreements in solitary wave characteristics. In addition, there were some background differences in the model predictions in relation to data. When these differences were taken into consideration, the predicted available potential energy levels agreed with the measured levels.

We have coupled the sound speed, derived from the two layer Strait of Messina hydrodynamic model predictions, with an acoustical parabolic equation (FEPE) model, and performed joint ocean-acoustic predictions. The effects of oceanographic parameters were considered in terms of their influence on joint oceanographic and acoustical predictions. The joint predictions were compared against acoustical calculations with the measured sound speed. Acoustic intensity

fields were compared with each other. The acoustic intensity fields for the tuned hydrodynamic model yielded similarities with the acoustic intensity fields obtained with the measured sound speed. There was agreement on the coarse scale acoustic intensity distributions. On finer scales there were some disagreement. Further work on predicting fine scale solitary wave structure is needed.

Our present work in the Strait of Messina is a first step towards the goal of joint ocean-acoustic predictions of solitary waves and their effects. We have established that we can predict the generation and propagation of solitary waves with nonhydrostatic models and that predictions show some close relation to data. One of the next steps in improving the predictions will be the bringing in of acoustics to guide the oceanographic parameter tuning to measured conditions. The use of acoustical intensity fields and their modal structures will enable the fine tuning (through parameter variations) of joint ocean-acoustic modelling to measured conditions. The comparisons of model-predicted acoustic transmission patterns and modal structures, with the analogue calculated from measured conditions, is a forthcoming approach for tuning the oceanographic parameters. Particular comparisons of modal structures bring out the differential between the large scale agreements and the small scale disagreements.

Acknowledgements

We particularly wish to thank Peter Brand and Angelo Rubino for giving us a version of their two-layer numerical model. Our thanks to Jurgen Sellschopp, who was chief scientist during the cruise, and who did an excellent job directing the gathering of the data by overcoming a constant stream of problems. The hydrographic data were obtained via the skilled data acquisition and processing abilities of the CTD/XCTD/XBT support staff of SACLANTCEN's Applied Oceanography Group, Ocean Engineering Department, Digital Computer Department, and the captain and crew of the NRV *Alliance*. This work was supported by the U.S. Office of Naval Research through the U.S. Naval Research Laboratory base program, PE 62435N. The U.S. Naval Research Laboratory provided technical management.

Appendix A. The Two-Layer Model

Brand et al. (1997), derived a weakly nonhydrostatic model for the Strait of Messina. A schematic depiction is shown in Figure 6. The momentum equations are expressed in terms of transport, $Q = u_i h_i W$, where u_i are the velocities, h_i the thickness of the layer, and W is the channel width. The continuity equations track the changes in the surface, ζ_1, and interface, ζ_2, elevations together with the transport variations. The equations are:

$$\frac{\partial Q_1}{\partial t} + \frac{\partial}{\partial x}(u_1 Q_1) + g h_1 W \frac{\partial \zeta_1}{\partial x} - A_h h_1 W \frac{\partial^2 \zeta_1}{\partial x^2} + W \frac{\tau_{\text{int}}}{\overline{\rho}} - \frac{h_1^2}{6} \frac{\partial^3 Q_2}{\partial x^2 \partial t} = 0, \tag{5}$$

$$\frac{\partial \zeta_1}{\partial t} + \frac{1}{W}\left(\frac{\partial Q_1}{\partial x} + \frac{\partial Q_2}{\partial x}\right) = 0,\ Q_1 = u_1 h_1 W, \tag{6}$$

$$\frac{\partial Q_2}{\partial t} + \frac{\partial}{\partial x}(u_2 Q_2) + g h_2 W \frac{\partial \zeta_1}{\partial x} + g' h_2 W \frac{\partial \zeta_2}{\partial x} - A_h h_2 W \frac{\partial^2 u_2}{\partial x^2} - W\left(\frac{\tau_{\text{int}} - \tau_{\text{bot}}}{\overline{\rho}}\right) - \left(\frac{h_2^2}{3} + \frac{h_2 h_1}{2}\right) \frac{\partial^3 Q_2}{\partial x^2 \partial t} = 0, \tag{7}$$

$$\frac{\partial \zeta_2}{\partial t} + \frac{1}{W} \frac{\partial Q_2}{\partial x} = 0, \tag{8}$$

where $\overline{\rho} = (\rho_1 + \rho_2)/2$, $g' = g \triangle \rho / \overline{\rho}$, $\triangle \rho = \rho_2 - \rho_1$, ρ is the density, τ is the stress, and A_h is the lateral viscosity. The last terms in Equations (5) and (7) describe the weakly nonhydrostatic effects in the Boussinesq approximation.

Appendix B. Parabolic Approximation Wave Equation

The Helmholtz wave equation for acoustic pressure is $\nabla^2 P(\vec{r}) + k^2 P(\vec{r}) = 0$, where $k(\vec{r}) = 2\pi f / C(\vec{r})$ is the acoustic wave number, f is the frequency, and $\vec{r}$ is the three-dimensional (3-D) position vector. In ocean acoustics it is customary to assume azimuthal symmetry. Thus, the 3-D Laplacian operator ∇^2 can be reduced to a 2-D operator in cylindrical coordinates of range, r, and depth, z:

$$\frac{\partial^2 P(r,z)}{\partial r^2} + \frac{1}{r}\frac{\partial P(r,z)}{\partial r} + \frac{\partial^2 P(r,z)}{\partial z^2} + k_0^2 n^2(r,z)\, P(r,z) = 0.$$

The acoustic wave number is expressed in terms of the index of refraction of the ocean environment, $n(r,z)$, as $k(r,z) = k_0 n(r,z)$, where k_0 is a reference wave number, and C_0 is the reference speed of sound in the ocean, i.e., $k_0 = 2\pi f / C_0$.

The complex pressure field, $P(r,z)$, is expressed in terms of a "reduced complex pressure field" $p(r,z)$, i.e., $P(r,z) = p(r,z)/\sqrt{r}$. After the cylindrical spreading term is removed, the reduced complex pressure equation becomes

$$\frac{\partial^2 p(r,z)}{\partial r^2} = -\left(k_0^2 n^2(r,z) + \partial^2/\partial z^2\right) p(r,z),$$

which can be factored into

$$\left[\frac{\partial}{\partial r} + ik_0\sqrt{(1+X)}\right]\left[\frac{\partial}{\partial r} - ik_0\sqrt{(1+X)}\right]p = 0.$$

Using the conventional notation, $X = k_0^{-2}\left(\partial^2/\partial z^2 + k^2 - k_0^2\right)$, the outgoing (propagating) acoustic pressure field can be written as

$$\frac{\partial p}{\partial r} = ik_0\sqrt{(1+X)}p.$$

The other factored equation represents the incoming acoustic energy which can be ignored due to causality requirements. With the removal of a common phase term, $\exp(ik_0 r)$, the resulting equation becomes the one-way parabolic equation (PE) approximation for ocean acoustics:

$$\frac{\partial p}{\partial r} = ik_0\left(-1 + \sqrt{(1+X)}\right)p.$$

The pseudo-differential operator term is approximated by a Padé approximation, $-1 + \sqrt{(1+X)} \cong \sum_{j=1}^{n} a_{j,n}X/(1 + b_{j,n}X)$. This gives

$$\frac{\partial p}{\partial r} = ik_0\sum_{j=1}^{n}\frac{a_{j,n}X}{1 + b_{j,n}X}p.$$

Higher levels of accuracy are obtained by keeping more terms in the Padé approximation. The FEPE ocean acoustic model is based on this PE approximation. The model allows the user to select the desired level of accuracy. Ocean features (e.g., internal waves) and rough ocean boundaries (e.g., sea surfaces, sea floors) are entered into the model by updating the environmental data as the model propagates the energy through the ocean. The FEPE model can accurately describe acoustic energy propagation throughout the entire ocean environment.

References

Apel, J.: 2001, A new analytical model for internal solitons in the ocean, Submitted to *J. Phys. Oceanogr.*

Apel, J., Finette, S., Orr, M., and Lynch, J.: 1998, The Dnoidal model for internal tides and solitons on the continental shelf, Report GOA 983.

Baines, P.: 1973, The generation of internal tides by flat-bump topography, *Deep Sea Res.* **20**, 179–205.

Baines, P.: 1982, On internal tide generation models, *Deep Sea Res.* **29**, 307–338.

Brand, P., Rubino, A., Alpers, W., and Backhaus, J.: 1997, Internal waves in the Strait of Messina studied by a numerical model and synthetic aperture radar images from the ERS-1 Satellites, *J. Phys. Oceanogr.* **27**(5), 648–663.

Brandt, P., Rubino, A., Quadfasel, D., Alpers, W., Sellschopp, J., and Fiekas, H.: 1998, Evidence for the influece of Atlantic-Ionian Stream fluctuations on the tidally induced internal dynamcis in the Strait of Messina, *J. Phys. Oceanogr.* **29**, 1071–1080.

Brickman, D. and Loder, J.: 1993, The energetics of the internal tide on northern Georges Bank, *J. Phys. Oceanogr.* **23**, 409–424.

Chin-Bing, S.A., King, D.B., Davis, J.A., and Evans, R.B. (eds.): 1993, *PE Workshop: Proceedings of the Second Parabolic Equation Workshop*, Naval Research Laboratory NRL/BE/7181-93-0001, US Government Printing Office.

Chin-Bing, S.A., King, D.B., and Murphy, J.E.: 1993, Numerical simulations of lower-frequency acoustic propagation and backscatter from solitary internal waves in a shallow water environment, in D.D. Ellis, J.R. Preston, and H.G. Urban, (eds.), *Ocean Reverberation*, Kluwer Academic Publishers, Dordrecht, The Netherlands.

Chin-Bing, S.A., King, D.B., Zingarelli, R.A., and Warn-Varnas, A.: 1999, A Search Algorithm for Resonance Anomalies (SARA), *1999 NRL Review*, Naval Research Laboratory, Washington, D.C.

Collins, M.D.: 1988a, Low-frequency, bottom-interacting pulse propagation in range-dependent oceans, *IEEE J. Ocean. Engng.* **13**, 222–228.

Collins, M.D.: 1988b, The time-domain solution of the wide-angle parabolic equation including the effects of sediment dispersion, *J. Acoust. Soc. Am.* **84**, 2114–2125.

Collins, M.D.: 1988c, FEPE user's guide, *NORDA TN-365*, Naval Research Laboratory, Stennis Space Center, MS.

Collins, M.D.: 1989a, A nearfield asymptotic analysis for underwater acoustics, *J. Acoust. Soc. Am.* **85**, 1107–1114.

Collins, M.D.: 1989b, Applications and time-domain solution of higher-order parabolic equations in underwater acoustics, *J. Acoust. Soc. Am.* **86**, 1097–1102.

Collins, M.D.: 1989c, A higher-order parabolic equation for wave propagation in an ocean overlying an elastic bottom, *J. Acoust. Soc. Am.* **86**, 1459–1464.

Collins, M.D.: 1990a, The rotated parabolic equation and sloping ocean bottoms, *J. Acoust. Soc. Am.* **87**, 1035–1037.

Collins, M.D.: 1990b, Benchmark calculations for higher-order parabolic equations, *J. Acoust. Soc. Am* **87**, 1535–1538.

Collins, M.D.: 1991, Higher-order Padé approximations for accurate and stable elastic parabolic equations with applications to interface wave propagation, *J. Acoust. Soc. Am.* **89**, 1050–1057.

Collins, M.D. and Westwood, E.K.: 1991, A higher-order energy-conserving parabolic equation for range-dependent ocean depth, sound speed, and density, *J. Acoust. Soc. Am.* **89**, 1068–1074.

Duda, T. and Preisig, J.: 1999, Acoustic mode coupling within internal solitary waves and wave groups, *Proceedings of the 1998 WHOI/IOS/ONR Internal Solitary Wave Workshop*, WHOI-99-07.

Essen, H.: 1976, Interpretation of observed fluctuations of the acoustic field in the SOFAR-channel as result of internal-wave disturbances, Ph.D. thesis, University of Hamburg.

Field, R.A.: 2000, Private communication.

Finette, S., Orr, M., Turgut, A., Apel, J., Badiey, M., Chui, C., Headrick, R. H., Kemp, J., Lynch, J., Newhall, A., von der Heydt, K., Pasewark, B., Wolf, S., and Tielbuerger, D.: 2000, Acoustic field variability induced by time evolving internal wave fields, *J. Acoust. Soc. Am.* **103**, 957–972.

Finette, S., Orr, M., and Apel, J.: 1999, Acoustic Field Fluctuations Caused by Internal Wave Soliton Packets, *Proceedings of the 1998 WHOI/IOS/ONR Internal Solitary Wave Workshop*, WHOI-99-07.

Gill, A.: 1982, *Atmosphere-Ocean Dynamics*, Academic Press, New York.

Hallock, Z.R., Small, J., George, J., Field, R., and Scott, J.: 2000, Shoreward internal wave propagation at the Malin Shelf edge, *Cont. Shelf Res.* **20**(15), 2045–2057.

King, D.B., Chin-Bing, S.A., and McGirr, R.W.: 1994, Effect of shallow water internal waves on broadband acoustic wave propagation, in D. Lee, and M. Shultz (eds.), *Environmental Acoustics: International Conference on Theoretical & Computational Acoustics*, Vol. II, World Scientific Press, Singapore, pp. 793–808.

Lamb, K.: 1994, Numerical experiments of internal wave generation by strong tidal flow across a finite amplitude bank edge, *J. Geophys. Res.* **99**(C1), 848–864.

Lamb, K.: 2000, Private communication.

New, A.: 1988, Internal tidal mixing in the Bay of Biscay, *Deep Sea Res.* **29**, 307–338.

Robinson, A., Sellschopp, J., Warn-Varnas, A., Leslie, W., Lozano, C., Haley, P., Anderson, L., and Lermusiaux, P.: 1999, The Atlantic Ionian Stream, *J. Marine Sci.* **20**, 129–156.

Sellschopp, J.: 1997, A towed CTD chain for high-resolution hydrography, *Deep Sea Res.* **44**, 147–165.

Shang, E., Wang, Y., and Ostrovsky, L.: 1999, Acoustical impact of inversion scheme of internal solitary waves, *Proceedings of the 1998 WHOI/IOS/ONR Internal Solitary Wave Workshop*, WHOI-99-07.

Sherwin, T.: 1991, A numerical investigation of semi-diurnal fluctuations in acoustic intensity at shelf edge, in J. Potter and A. Warn-Varnas (eds.) *Ocean Variability & Acoustic Propagation*, Kluwer Academic Publishers, Dordrecht, The Netherlands.

Small, J., Hallock, Z., Pavey, G., and Scott, J.: 1999, Observations of large amplitude internal at the Malin Shelf edge during SESAME 1995, *Cont. Shelf Res.* **19**, 1389–1436.

The Shelfbreak PRIMER Group: 1997, Shelfbreak PRIMER – An integrated acoustic and oceanographic field study in the middle Atlantic bight, in R. Zhang and J.X. Zhou, (eds.), *Shallow-Water Acoustics*, China Ocean Press.

The SWARM Group: 1997, An overview of the 1995 SWARM shallow water internal wave acoustic scattering experiment, in Apel et al., *IEEE J. Oceanic Engng.* **22**(3), 465–500.

Tielburger, D., Finette, S., and Wolf, S.: 1997, Acoustic field propagation through an internal wave field in a shallow water waveguide, *J. Acoust. Soc. Am.* **101**, 789–808.

Tieman, C., Worcester, P., Cornuelle, B., and Send, U.: 1999, Effects of Internal Waves and Bores on Acoustic Transmissions in the Strait of Gibraltar, *Proceedings of the 1998 WHOI/IOS/ONR Internal Solitary Wave Workshop*, WHIO-99-07.

Warn-Varnas, A., Chin-Bing, S.A., King, D.B., Piacsek, S., and MacNaughton, A.: 1999, Modelling the effects of solitons on acoustics, *Proceedings of the 1998 WHOI/IOS/ONR Internal Solitary Wave Workshop*, WHOI-99-07.

Zhou, J.X., Zhang, X.Z., and Rogers, P.H.: 1991, Resonant interaction of sound wave with internal solitons in coastal zone, *J. Acoust. Soc. Am.* **90**(4), 2042–2054.